THESIS FOR THE DEGREE OF LICENTIATE IN ENGINEERING

Large eddy simulation of transonic flow with shock wave/turbulent boundary layer interaction

CHRISTIAN WOLLBLAD

Division of Thermo and Fluid Dynamics

CHALMERS UNIVERSITY OF TECHNOLOGY

Göteborg, Sweden, 2004

Large eddy simulation of transonic flow with shock wave/turbulent boundary layer interaction

CHRISTIAN WOLLBLAD

ISSN 1101-9972
ISRN CTH-TFD-PB-04/07

Division of Thermo and Fluid Dynamics
Chalmers University of Technology
SE-412 96 Göteborg
Sweden
Phone: +46-(0)31-772 1400
Fax: +46-(0)31-180976

Printed at Chalmers Reproservice
Göteborg, Sweden, 2004

Large eddy simulation of transonic flow with shock wave/turbulent boundary layer interaction

Christian Wollblad
wollblad@tfd.chalmers.se
Division of Thermo and Fluid Dynamics
Chalmers University of Technology
SE-412 96 Göteborg
Sweden

Abstract

Large eddy simulations (LES) of shock wave/turbulent boundary layer interaction (SWTBLI) have been carried out. The flow configuration was that of transonic flow over a bump with inlet Mach number 0.75 and maximum Mach number 1.27. The Reynolds number based on the free stream velocity and inlet momentum loss thickness was 2400. The Favre filtered Navier-Stokes equations were solved using a finite volume solver. The convective fluxes were discretized with a low dissipative third order upwind scheme and the viscous fluxes were discretized using a second-order central scheme. The subgrid stresses were modeled using a compressible version of Smagorinsky's model. Time marching was performed using a low-storage three-stage Runge-Kutta scheme. In each stage of the Runge-Kutta scheme, cells close to a solid wall were pre-conditioned using a newly developed pre-conditioning method saving up to 60 % of the computational time.

The computational domain was discretized using block structured grids, the largest one with approximately $6.7 \cdot 10^6$ nodes. Time dependent inlet data constructed from measurements and DNS computations were used and the computations were performed on parallel computers using message-passing interface MPI. Computations from three different grids were compared to ensure good enough resolution and wide enough domain to contain all structures of the flow.

PDF of the skin friction coefficient and large amplification of the Reynolds stresses suggest strong separation at the SWTBLI. Still, no shock movement could be detected, which is in contradiction with measurements made at KTH. The form factor of the incoming boundary layer never exceeds 2 which is much lower than the conventional condition for separation. By fast Fourier transforms of autocorrelations, characteristic frequencies could be found in the separated region. These frequencies could all be found also in the autocorrelations of the incoming boundary layer. The bursting frequency of the incoming boundary layer was found to be in agreement with the outer scaling $0.14U_\infty/\delta_{99}$, but it could not be detected anywhere in the separated region.

Acknowledgments

This work was conducted at the Division of Thermo and Fluid Dynamics at Chalmers University of Technology and sponsored by the Swedish Energy Agency (STEM).

I would like to thank my supervisors Lars Davidson and Lars-Erik Eriksson for sharing there great knowledge and for showing such exceptional patience with my stubbornness.

Many thanks to all other employees on Thermo and Fluid Dynamics for contributing with valuable ideas and creating a stimulating working atmosphere. Special thanks to Associate Professor Gunnar Johansson for always being able to spare a few minutes and to Mattias Billson and Niklas Andersson for helping me with the code.

The National Supercomputer Center, NSC, is gratefully acknowledged for providing computational resources.

Finally I would like to thank my beloved fiancée Maria for her constant and invaluable support.

Nomenclature

Roman letters

Q	total fluxes
F_i	inviscid fluxes
F_{vi}	viscous fluxes
x_i	space coordinates
u_i	velocity in space direction i
t	time
p	pressure
e_0	total internal energy
h_0	total enthalpy
q_i	heat transfer in space direction i
T	temperature
Pr	Prandtl number
e	internal energy
h	enthalpy
c_p and c_v	specific heats
r_i	distance variable
S_{ij}	the strain rate tensor
C_R and C_I	filter constants
Pr_T	turbulent Prandtl number
$\mathcal{Q}$	total fluxes (filtered and modeled)
$\mathcal{F}_i$	inviscid fluxes (filtered and modeled)
$\mathcal{F}_{vi}$	viscous fluxes (filtered and modeled)
a	speed of sound
w_i	characteristic variables, $i = 1, 2, 3, 4, 5$
$\vec{q}$	primitive variables

f	frequency
P_h	power spectrum
U	streamwise velocity
M	Mach number
$\langle u_i u_j \rangle$	(resolved) Reynolds stresses
c_f	skin friction coefficient
P('event')	probability for 'event' to occure
K	acceleration parameter
H	form factor
I_M	indicator function

Greak letters

ρ	density
δ_{ij}	Kronecker's delta
μ	dynamic viscosity
τ_{ij}	viscous stress tensor
Δ	filter width
λ_i	eigenvalue to charateristic variable i
γ	recovery factor
τ_w	wall friction
ν	kinematic viscosity
σ	standard deviation

Subscripts

∞	free-stream condition
w	wall condition

Superscripts

$\bar{}$	space filtered quantity
$\tilde{}$	favre filtered quantity
$''$	deviation from favre averaged value
A	quantity evaluated at cell face
L	left upwinding quantity
R	right upwinding quantity
CF	cell face
DP	boundary data point
S	point on a surface
$'$	fluctuation from time average
$+$	wall friction unit

Conventions

Nodes and cells.	The grids, which are structured grids, are built up from nodes. A cell consists of eight nodes, one in each corner. The flow data is represented as averages over these cells.

Contents

Chapter 1

Introduction

Shock wave/turbulent boundary layer interactions (SWTBLI) commonly arise in the field of turbo machinery, aero-space applications and on the exterior of high-speed aircrafts. In all of these cases, shock wave boundary layer interaction can significantly change the flow and hence the physical load enforced by it. Also, the performance of the object studied can be significantly altered if shocks and boundary layer separations do not occur where expected. It is therefore desirable to have reliable and effective prediction tools for SWTBLI. But today, no such tools exist. Instead, compromises often have to be made in performance to ensure dependability.

Many experimental studies have been performed, but most of them are done using intrusive methods [1] or methods that only give a qualitative picture of the flow, like Schlieren photographs. Thus, from older experiments, only basic understanding of the phenomena has been achieved [2]. There are of course newer techniques such as PIV and LDV which can give deeper understanding [3], specially when combined with numerical simulations (see for example ref. [4]).

Quite a few calculations done on SWTBLI can be found, but most of them are from Reynolds averaged Navier-Stokes (RANS) computations since since the high computational cost long has hindered more advanced calculations. There are several reasons why RANS methods at best give fair results. Firstly, flows of the kind considered here include both separation and recirculation, phenomenas hard to capture with RANS. Secondly, flows with SWTBLI often feature low frequent shock motions which cannot be captured by RANS. See for example reference [1] and reference [5] for more detailed discussions. In resent years, large eddy simulations (LES) [6, 7] have been performed showing much better agreement with experiments than RANS calculations [5], but the references are few.

In this work, transonic flow over a bump (see chapter 4) is studied.

The goal of the study is twofold. The first goal is to investigate the flow properties of SWTBLI in a transonic flow to contribute to a deeper understanding of such flow phenomena. That investigation is made both by experiments performed at KTH (see ref. [8] and [9]) and by numerical simulations presented here. The investigation will result in a data base which shall be used to reach the second goal: Development of new computational tools suitable for transonic flows. For the purpose of developing new computational tools, it is of utmost importance that the investigations are made using methods that are as accurate as possible. Considering the shortcoming of RANS, and the absurdly high computational costs for direct numerical simulations (DNS), LES was selected for this work.

Chapter 2

LES numerics

2.1 Governing equations

The solver for the Navier-Stokes equations is based on the G3D series of codes developed by Lars-Erik Eriksson [10]. The conservative forms of the continuity, momentum and energy equations governing viscous compressible flow, solved by the code, can be written in the form:

$$\frac{\partial}{\partial t}Q + \frac{\partial}{\partial x_i}(F_i - F_{vi}) = 0 \tag{2.1}$$

where

$$Q = \begin{bmatrix} \rho \\ \rho u_1 \\ \rho u_2 \\ \rho u_3 \\ \rho e_0 \end{bmatrix} \quad F_i = \begin{bmatrix} \rho u_i \\ \rho u_1 u_i + p\delta_{1i} \\ \rho u_2 u_i + p\delta_{2i} \\ \rho u_3 u_i + p\delta_{3i} \\ \rho h_0 u_i \end{bmatrix} \quad F_{vi} = \begin{bmatrix} 0 \\ \tau_{1i} \\ \tau_{2i} \\ \tau_{3i} \\ \tau_{ji}u_j - q_i \end{bmatrix}$$

where in turn

$$\tau_{ij} = -\frac{2}{3}\mu\frac{\partial u_m}{\partial x_m}\delta_{ij} + \mu\left(\frac{\partial u_i}{\partial x_j} + \frac{\partial u_j}{\partial x_i}\right) \tag{2.2}$$

$$q_i = -\frac{\mu c_p}{Pr}\frac{\partial T}{\partial x_i} \tag{2.3}$$

To close the equation system, calorically perfect gas is assumed, i.e. the following relations can be used

$$p = \rho RT \tag{2.4}$$

$$e = c_v T \tag{2.5}$$

$$h = c_p T \tag{2.6}$$

$$c_v = c_p - R \tag{2.7}$$

and c_p and μ are constant. R is the ideal gas constant.

2.2 Large eddy formulation

A filtered quantity $\overline{\Phi}$ is obtained from the unfiltered quantity Φ by the integral operation

$$\overline{\Phi}(x_i,t) = \int_{\mathcal{R}^3} G(r_i,x_i)\Phi(x_i - r_i, t)\, dr_1 dr_2 dr_3 \tag{2.8}$$

For each x_i, the filter function $G(r_i,x_i)$ has a maximum at $r_i = 0$ and $G(r_i,x_i) \leq G(0,x_i)\ \forall r_i \in \mathcal{R}^3$. Furthermore, $G(r_i,x_i)$ is normalized so that

$$\int_{\mathcal{R}^3} G(r_i,x_i)\, dr_1 dr_2 dr_3 = 1\ \forall x_i \in \Omega \tag{2.9}$$

where Ω is the computational domain. Hence, for a specific x_i, $\overline{\Phi}(x_i,t)$ will be a weighted average of all values within some volume centered at x_i. The size of the volume can be represented by some length scale Δ which is called the filter width.

The large eddy formulation is obtained by applying the filter operation to the governing equations. The result, however, is often written using the Favre notation since the results then look very similar to the unfiltered equations. The Favre averaged quantity $\tilde{\Phi}$ is related to $\overline{\Phi}$ by

$$\widetilde{\Phi} = \frac{\overline{\rho\Phi}}{\bar{\rho}} \tag{2.10}$$

and to the unfiltered quantity Φ by

$$\Phi = \widetilde{\Phi} + \Phi'' \tag{2.11}$$

$\tilde{\Phi}$ is the resolved part of Φ and Φ'' the unresolved part. Since $G(r_i,x_i)$ is often related to the computational grid in some way, Φ'' is called the subgrid fluctuations of Φ.

The modeling approach used in the code is very similar to the one described by Erlebacher et.al. Details about the modeling assumptions can be found in reference [11].

2.2.1 The continuity equation

Upon filtering, the continuity equation becomes

$$\frac{\partial\bar{\rho}}{\partial t} + \frac{\partial(\bar{\rho}\tilde{u}_i)}{\partial x_i} = 0 \tag{2.12}$$

which needs no modeling.

2.2.2 The momentum equations

Applying the space filter to the momentum equations gives the result

$$\frac{\partial(\bar{\rho}\tilde{u}_i)}{\partial t} + \frac{\partial(\bar{\rho}\tilde{u}_i\tilde{u}_j)}{\partial x_j} = -\frac{\partial \bar{p}}{\partial x_i} + \frac{\partial \bar{\tau}_{ij}}{\partial x_j} + \frac{\partial \tau_{ij}^{SGS}}{\partial x_j} \tag{2.13}$$

Only the last term on the right hand side in equation (2.13) needs modeling. It can be written as:

$$\frac{\partial \tau_{ij}^{SGS}}{\partial x_j} = \frac{\partial}{\partial x_j}\left(-\bar{\rho}(\widetilde{\tilde{u}_i\tilde{u}_j} - \tilde{u}_i\tilde{u}_j) - \bar{\rho}(\widetilde{\tilde{u}_i u_j''} + \widetilde{u_i''\tilde{u}_j}) - \bar{\rho}\widetilde{u_i''u_j''}\right) \tag{2.14}$$

τ_{ij}^{SGS} is called the subgrid stress tensor and is in the code modeled by

$$\tau_{ij}^{SGS} = 2C_R\bar{\rho}\Delta^2\Pi_{\tilde{S}}^{\frac{1}{2}}(\tilde{S}_{ij} - \frac{1}{3}\tilde{S}_{mm}\delta_{ij}) - \frac{2}{3}C_I\bar{\rho}\Delta^2\Pi_{\tilde{S}}\delta_{ij} \tag{2.15}$$

where

$$\tilde{S}_{ij} = \frac{1}{2}\left(\frac{\partial \tilde{u}_i}{\partial x_j} + \frac{\partial \tilde{u}_j}{\partial x_i}\right) \tag{2.16}$$

$$\Pi_{\tilde{S}} = \tilde{S}_{mn}\tilde{S}_{mn} \tag{2.17}$$

C_R and C_I are user-defined constants.

2.2.3 The energy equation

When the energy equation is filtered, the following expression is obtained:

$$\frac{\partial(\bar{\rho}\tilde{e}_0)}{\partial t} + \frac{\partial(\bar{\rho}\tilde{h}_0\tilde{u}_i)}{\partial x_i} = -\frac{\partial \bar{q}_i}{\partial x_i} + \frac{\partial(\overline{\tau_{ij}u_j})}{\partial x_i} + \frac{\partial \Phi_i}{\partial x_i} \tag{2.18}$$

In equation (2.18) there are two terms that need modeling, the derivatives of $\overline{\tau_{ij}u_j}$ and the last term on the right hand side which written out is

$$\begin{aligned}\frac{\partial \Phi_i}{\partial x_i} \;=\; & \frac{\partial}{\partial x_i}\left(q_i^{SGS} + \bar{\rho}\tilde{u}_k\widetilde{u_k''u_j''} + \frac{1}{2}\bar{\rho}\widetilde{\tilde{u}_k\tilde{u}_k u_j''} + \frac{1}{2}\bar{\rho}\widetilde{u_k''u_k''u_j''}\right. \\ & +\bar{\rho}\left(\frac{1}{2}\left(\widetilde{\tilde{u}_k\tilde{u}_k\tilde{u}_j} - \widetilde{\tilde{u}_k\tilde{u}_k}\tilde{u}_j\right) + \left(\widetilde{\tilde{u}_k u_k''\tilde{u}_j} - \widetilde{\tilde{u}_k u_k''}\tilde{u}_j\right) + \right. \\ & \left.\left.\frac{1}{2}\left(\widetilde{u_k''u_k''\tilde{u}_j} - \widetilde{u_k''u_k''}\tilde{u}_j\right) + \left(\widetilde{\tilde{u}_k u_k''u_j''} - \tilde{u}_k\widetilde{u_k''u_j''}\right)\right)\right)\end{aligned} \tag{2.19}$$

where

$$q_i^{SGS} = \bar{\rho}c_p\left(\widetilde{\tilde{T}\tilde{u}_i} - \tilde{T}\tilde{u}_i + \widetilde{T''\tilde{u}_i} + \widetilde{\tilde{T}u_i''} + \widetilde{T''u_i''}\right) \tag{2.20}$$

represents the subgrid heat fluxes and is modeled using

$$q_i^{SGS} = -c_p\frac{C_R}{Pr_T}\bar{\rho}\Delta^2\Pi_{\tilde{S}}^{\frac{1}{2}}\frac{\partial \tilde{T}}{\partial x_i} \tag{2.21}$$

Pr_T is the turbulent Prandtl number which is given by the user. $\widetilde{u_k'' u_j''}$ is modeled with τ_{kj}^{SGS}. The differences i triple correlation and the term $\bar{\rho}\widetilde{u_k'' u_k'' u_j''}$ can all argued to be small and are thus neglected. The term $\bar{\rho}\widetilde{\tilde{u}_k \tilde{u}_k u_j''}$ is also discarded. Finally, $\overline{\tau_{ij} u_j}$ in equation (2.18) is replace by $\bar{\tau}_{ij}\tilde{u}_j$.

2.2.4 Filter and constants

There are several possible choices of filter function $G(r_i, x_i)$ (see for example ref. [12]), but most common is a box filter of grid cell size, which is used in the current case. The filtering operation is then performed implicitly in the code by the discretization scheme.

The filter width was constant and set to $4 \cdot 10^{-5}$, which is approximately equal to $(\Delta x \Delta y \Delta z)^{1/3}$ for the smallest grid cells. There are evidence that SGS-models with only one length scale are not functional in areas with large an-isotropy, for example in separated regions [1]. But such a problem can be helped if the grid is fine enough in the critical regions.

The filter constants C_R and C_I were set to 0.012 and 0.0066 respectively and the value 0.7 was chosen for the turbulent Prandtl number.

2.3 Space discretization

For spatial discretization, one scheme is used for the inviscid terms and another for the viscous terms. The filtered and modeled version of equation (2.1) can be written on the form

$$\frac{\partial \mathcal{Q}}{\partial t} + \frac{\partial}{\partial x_i}(\mathcal{F}_i - \mathcal{F}_{vi}) = 0 \tag{2.22}$$

where

$$\mathcal{Q} = \begin{bmatrix} \bar{\rho} \\ \overline{\rho u}_1 \\ \overline{\rho u}_2 \\ \overline{\rho u}_3 \\ \overline{\rho e}_0 \end{bmatrix}$$

$\mathcal{F}_i$ and $\mathcal{F}_{vi}$ can be identified as the filtered and modeled counterpart of the inviscid and viscous part of the total flux and are also known as the convective and the diffusive fluxes. Equation (2.22) is discretized on a structured non-orthogonal mesh using the Finite Volume Method (FVM). Integrating equation (2.22) over some arbitrary volume Ω gives

$$\int_\Omega \frac{\partial \mathcal{Q}}{\partial t}\, dV + \int_\Omega \frac{\partial}{\partial x_i}(\mathcal{F}_i - \mathcal{F}_{vi})\, dV = 0 \tag{2.23}$$

Taking Ω to be a cell in the grid and introducing $\mathcal{S}_j = n_j S$ as the face area normal vector and $\overline{\mathcal{Q}}$ as the cell average of $\mathcal{Q}$ over Ω, Gauss theorem can be used to rewrite equation (2.23) as

$$\frac{\partial \overline{\mathcal{Q}}}{\partial t} V + \int_{\partial\Omega} (\mathcal{F}_i - \mathcal{F}_{vi})\, d\mathcal{S}_i = 0 \tag{2.24}$$

The integral of the fluxes is approximated by

$$\int_{\partial\Omega} (\mathcal{F}_i - \mathcal{F}_{vi})\, d\mathcal{S}_j = \sum_{k=1}^{allfaces} (\mathcal{F}_i^k - \mathcal{F}_{vi}^k) \cdot \mathcal{S}_i^k \tag{2.25}$$

where $\mathcal{F}_i^k$ and $\mathcal{F}_{vi}^k$ are the cell face average of the convective and diffusive fluxes respectively and $\mathcal{S}_i^k$ is the area of the cell faces. In total, the finite volume formulation of equation (2.22) is

$$\frac{\partial \overline{\mathcal{Q}}}{\partial t} V + \sum_{k=1}^{allfaces} (\mathcal{F}_i^k - \mathcal{F}_{vi}^k) \cdot \mathcal{S}_i^k = 0 \tag{2.26}$$

2.3.1 Convective fluxes

From here on, it will assumed that the grid is Cartesian. If it is not, it can be transformed into one (see for example ref. [13]). All formulations will then apply to the transformed equations instead. This transformation is actually done in the code but will not be described here.

A purely inviscid flow is governed by Euler's equations, which, if the flow is smooth, can be written on the form

$$\frac{\partial Q}{\partial t} + \frac{\partial F_i}{\partial Q}\frac{\partial Q}{\partial x_i} = 0 \tag{2.27}$$

If only a small area is considered, the flux Jacobian matrices, $(\partial F_i)/(\partial Q)$ can be regarded as constants and the linear relation

$$\frac{\partial Q}{\partial t} + \left(\frac{\partial F_i}{\partial Q}\right)_0 \frac{\partial Q}{\partial x_i} = 0 \tag{2.28}$$

is obtained where the subscript 0 denotes evaluation at a reference state. Now assume that this reference state is perturbed with planar waves. These waves are in a plane which have a normal vector $[\alpha_1, \alpha_2, \alpha_3]$ with $\alpha_i \alpha_i = 1$. Aligning the coordinate system with this vector will transform equation (2.28) into

$$\frac{\partial Q}{\partial t} + \hat{A}_0 \frac{\partial Q}{\partial \xi} = 0 \tag{2.29}$$

where

$$\hat{A}_0 = \alpha_i \left(\frac{\partial F_i}{\partial Q} \right)_0$$

and ξ is the coordinate in the direction of $\vec{\alpha}$ given by

$$\xi = \alpha_i x_i$$

Equation (2.29) is a system of one-dimensional linear equations describing propagation of waves along the ξ-axis. The matrix $\hat{A}_0$ may be diagonalized by its eigenspace vector T using some standard eigendecomposition procedure. This will give

$$T\hat{A}_0 T^{-1} = \Lambda = diag(\lambda_1, \lambda_2, \lambda_3, \lambda_4, \lambda_5) \tag{2.30}$$

The eigenvalues $\lambda_1, \lambda_2, \lambda_3, \lambda_4, \lambda_5$ are exactly given by

$$\begin{array}{rcl} \lambda_1 & = & \alpha_i u_i \\ \lambda_2 & = & \lambda_1 \\ \lambda_3 & = & \lambda_1 \\ \lambda_4 & = & \lambda_1 + a\sqrt{\alpha_i \alpha_i} \\ \lambda_5 & = & \lambda_1 - a\sqrt{\alpha_i \alpha_i} \end{array} \tag{2.31}$$

where a is the speed of sound. Using the characteristic variables defined by $W = T^{-1}Q$, equation (2.29) can be written as the uncoupled system

$$\frac{\partial W}{\partial t} + \Lambda \frac{\partial W}{\partial \xi} = 0 \tag{2.32}$$

which describe the transport of the characteristic variables w_i in the ξ-direction. Each w_i can be interpreted as a wave carrying some kind of information. w_1 is an entropy wave, w_2 and w_3 vorticity waves and w_4 and w_5 can be interpreted as sound waves. Each wave transports its information with a characteristic speed described by the corresponding eigenvalue λ_i.

When calculating the fluxes, the code uses the flow variables on primitive form:

$$\vec{q} = \begin{bmatrix} \bar{\rho} \\ \tilde{u}_1 \\ \tilde{u}_2 \\ \tilde{u}_3 \\ \bar{p} \end{bmatrix} \tag{2.33}$$

which are obtained from the conservative variables with second order accuracy. $\bar{p}$ is an approximation calculated by $\bar{p} = (\gamma - 1)(\overline{\rho e_0} + \bar{\rho}(\tilde{u}^2 + \tilde{v}^2 + \tilde{w}^2))$.

To calculate the inviscid flux over a cell face A, data from four cells are needed. The arrangement is shown in figure 2.1. The cell face A is

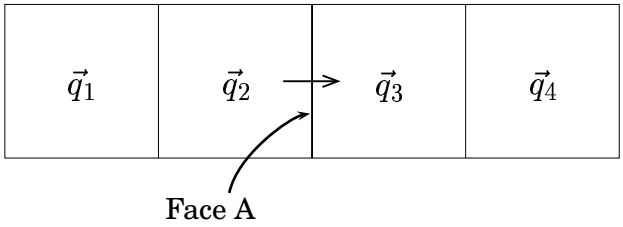

Figure 2.1: Cells used to obtain the inviscid fluxes across the cell face A.

described by the normal vector $\mathcal{S}_i$. The outline is to use this $\mathcal{S}_i$ as ξ in equation (2.29) to obtain the characteristic speeds:

$$\begin{aligned} \lambda_1 &= \tilde{u_i}^A \mathcal{S}_i \\ \lambda_2 &= \lambda_1 \\ \lambda_3 &= \lambda_1 \\ \lambda_4 &= \lambda_1 + a^A \sqrt{\mathcal{S}_i \mathcal{S}_i} \\ \lambda_5 &= \lambda_1 - a^A \sqrt{\mathcal{S}_i \mathcal{S}_i} \end{aligned} \tag{2.34}$$

where superscript A denotes that the variable is obtained from $\vec{q}^A = 0.5(\vec{q}_2 + \vec{q}_3)$. The sign of each of the eigenvalues determines whether the information is traveling from left to right or from right to left. $\lambda_i > 0$ indicates the former while $\lambda_i < 0$ indicates the latter case. A left and a right upwinding flux for the cell face A are computed from

$$\begin{aligned} \vec{q}^L &= C_1\vec{q}_1 + C_2\vec{q}_2 + C_3\vec{q}_3 + C_4\vec{q}_4 \\ \vec{q}^R &= C_4\vec{q}_1 + C_3\vec{q}_2 + C_2\vec{q}_3 + C_1\vec{q}_4 \end{aligned} \tag{2.35}$$

The coefficients C_1, C_2, C_3 and C_4 define the upwinding scheme and are here given by

$$(C_1, C_2, C_3, C_4) = \left(-\frac{1}{12} - \epsilon, \frac{7}{12} + 3\epsilon, \frac{7}{12} - 3\epsilon, -\frac{1}{12} + \epsilon \right) \tag{2.36}$$

which along with $\epsilon = 1/100$ gives a scheme that is third order accurate in terms of dissipation, but still fourth order in terms of dispersion. By determination of the sign of the corresponding eigenvalue, the characteristic variables are obtained by using data from either left or right upwinding, i.e. if $\lambda_i > 0$, $\vec{q}^L$ is used and if $\lambda_i \leq 0$, $\vec{q}^R$ is used. The

characteristic variables are given by

$$\begin{aligned}
w_1 &= \bar{\rho}^{L/R} - \frac{\bar{p}^{L/R}}{(a^A)^2} \\
w_2 &= \frac{\mathcal{S}_1\tilde{u}_2^{L/R} - \mathcal{S}_2\tilde{u}_1^{L/R}}{\sqrt{\mathcal{S}_1\mathcal{S}_1 + \mathcal{S}_2\mathcal{S}_2}} \\
w_3 &= \frac{1}{\sqrt{\mathcal{S}_i\mathcal{S}_i}}\left((\sqrt{\mathcal{S}_1\mathcal{S}_1 + \mathcal{S}_2\mathcal{S}_2})\tilde{u}_3^{L/R} - \mathcal{S}_3\left(\frac{\mathcal{S}_1\tilde{u}_1^{L/R} + \mathcal{S}_2\tilde{u}_2^{L/R}}{\sqrt{\mathcal{S}_1\mathcal{S}_1 + \mathcal{S}_2\mathcal{S}_2}}\right)\right) \\
w_4 &= \frac{1}{2}\left(\frac{\bar{\rho}^A}{a^A}\frac{\mathcal{S}_i\tilde{u}_i^{L/R}}{\sqrt{\mathcal{S}_i\mathcal{S}_i}} + \frac{\bar{p}^{L/R}}{(a^A)^2}\right) \\
w_5 &= \frac{1}{2}\left(-\frac{\bar{\rho}^A}{a^A}\frac{\mathcal{S}_i\tilde{u}_i^{L/R}}{\sqrt{\mathcal{S}_i\mathcal{S}_i}} + \frac{\bar{p}^{L/R}}{(a^A)^2}\right)
\end{aligned} \tag{2.37}$$

The characteristic variables are transformed back to face approximations (denoted $\hat{}$) of the solution variables on primitive form using

$$\begin{aligned}
\hat{\rho} &= w_1 + w_4 + w_5 \\
\hat{u}_1 &= -\frac{\mathcal{S}_2 w_2}{\sqrt{\mathcal{S}_1\mathcal{S}_1 + \mathcal{S}_2\mathcal{S}_2}} - \frac{\mathcal{S}_1}{\sqrt{\mathcal{S}_i\mathcal{S}_i}}\left(\frac{\mathcal{S}_3 w_3}{\sqrt{\mathcal{S}_1\mathcal{S}_1 + \mathcal{S}_2\mathcal{S}_2}} - \frac{a^A}{\bar{\rho}^A}(w_4 + w_5)\right) \\
\hat{u}_2 &= \frac{\mathcal{S}_2 w_2}{\sqrt{\mathcal{S}_1\mathcal{S}_1 + \mathcal{S}_2\mathcal{S}_2}} - \frac{\mathcal{S}_1}{\sqrt{\mathcal{S}_i\mathcal{S}_i}}\left(\frac{\mathcal{S}_3 w_3}{\sqrt{\mathcal{S}_1\mathcal{S}_1 + \mathcal{S}_2\mathcal{S}_2}} - \frac{a^A}{\bar{\rho}^A}(w_4 + w_5)\right) \\
\hat{u}_3 &= \frac{1}{\sqrt{\mathcal{S}_i\mathcal{S}_i}}\left(\frac{w_3}{\sqrt{\mathcal{S}_1\mathcal{S}_1 + \mathcal{S}_2\mathcal{S}_2}} + \frac{\mathcal{S}_3 a^A}{\bar{\rho}^A}(w_4 + w_5)\right) \\
\hat{p} &= (a^A)^2(w_4 + w5)
\end{aligned} \tag{2.38}$$

These cell face values are then used in the evaluation of $\mathcal{F}_i^k$ in equation (2.26).

2.3.2 Diffusive fluxes

The diffusive fluxes are for each cell face treated with a second order central scheme with no upwinding. That is, if treating the cell face between cell i, j, k and cell $i+1, j, k$, assuming Cartesian net, the derivatives are calculated by

$$\begin{aligned}
\frac{\partial\vec{q}}{\partial x} &= \frac{\vec{q}_{i+1,j,k} - \vec{q}_{i,j,k}}{x_{i+1,j,k} - xi, j, k} \\
\frac{\partial\vec{q}}{\partial y} &= \frac{1}{4}\left(\frac{\vec{q}_{i,j+1,k} - \vec{q}_{i,j-1,k}}{y_{i,j+1,k} - y_{i,j-1,k}}\right) + \frac{1}{4}\left(\frac{\vec{q}_{i+1,j+1,k} - \vec{q}_{i+1,j-1,k}}{y_{i+1,j+1,k} - y_{i+1,j-1,k}}\right) \\
\frac{\partial\vec{q}}{\partial z} &= \frac{1}{4}\left(\frac{\vec{q}_{i,j,k+1} - \vec{q}_{i,j,k-1}}{z_{i,j,k+1} - z_{i,j,k-1}}\right) + \frac{1}{4}\left(\frac{\vec{q}_{i+1,j,k+1} - \vec{q}_{i+1,j,k-1}}{z_{i+1,j,k+1} - z_{i+1,j,k-1}}\right)
\end{aligned} \tag{2.39}$$

where i, j and k denote the cell indexes in the x, y and z direction respectively. These results are then also used in equation (2.26).

2.4 Extra diffusion for strong shocks

In the case of strong shocks, the scheme previously described cannot handle the discontinuity. Instead, instabilities cause the calculations to diverge. To counter this, extra shock handling diffusion is added. As the flux are calculated an extra term with the form

$$C_{PD} \max\left[\frac{|\bar{p}_1 - 2\bar{p}_2 + \bar{p}_3|}{\bar{p}_1 + 2\bar{p}_2 + \bar{p}_3}, \frac{|\bar{p}_2 - 2\bar{p}_3 + \bar{p}_4|}{\bar{p}_2 + 2\bar{p}_3 + \bar{p}_4}\right] \max[\lambda_i](\bar{\mathcal{Q}}_3 - \bar{\mathcal{Q}}_2) \qquad (2.40)$$

is added to the right hand side of equation (2.26). In equation (2.40) the indexes of $\bar{p}$ and $\bar{\mathcal{Q}}$ refer to figure 2.1 and the index i on λ refers to equation (2.34). The spectral radius $\max[\lambda_i]$ accounts for aspects of the flow other than the pressure. C_{PD} is a user-defined constant which, if shocks are expected, is normally set to 0.4. In this case, however, C_{PD} could be set to 0.05 only.

2.5 Time stepping

Time stepping is performed by a a three-stage low-storage Runge-Kutta method combined with a semi-implicit precondition scheme. The general outline reassembles the ordinary use of the Runge-Kutta method which is as follow. By using the latest known data, $\mathcal{Q}^n$ that is valid for time step n, $\frac{\partial \mathcal{Q}}{\partial t}$ is approximated using the methods described in section 2.3. This term is denoted $\left(\frac{\partial \mathcal{Q}}{\partial t}\right)^n$. The three stages are then

$$\begin{aligned} \mathcal{Q}^* &= \mathcal{Q}^n + \Delta t \left(\tfrac{\partial \mathcal{Q}}{\partial t}\right)^n \\ \mathcal{Q}^{**} &= \tfrac{1}{2}\left(\mathcal{Q}^n + \mathcal{Q}^* + \Delta t \left(\tfrac{\partial \mathcal{Q}}{\partial t}\right)^*\right) \\ \mathcal{Q}^{n+1} &= \tfrac{1}{2}\left(\mathcal{Q}^n + \mathcal{Q}^{**} + \Delta t \left(\tfrac{\partial \mathcal{Q}}{\partial t}\right)^{**}\right) \end{aligned} \qquad (2.41)$$

where Δt denotes the time step size between time step n and $n+1$. Super scripts $*$ and $**$ denotes sub time-steps. More on Runge-Kutta schemes can be found in reference [14].

The difference lies in that cells close to a solid wall is pre-conditioned. The pre-conditioning is obtained by Taylor expansion of the implicit time stepping formulation of equation (2.26). Close to a wall, the CFL-number is totally dominated by sound waves in the wall normal direction. This information can be used to decouple the obtained equation system in all but the wall normal direction. The preconditioning method is described in reference [15] which is included in this thesis.

2.6 Boundary conditions

Four types of boundary conditions used in the computations of this work. Two of them will be described here.

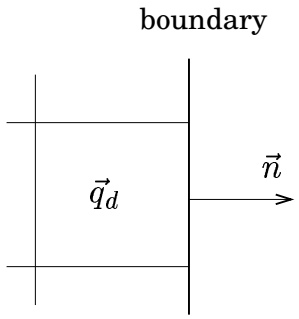

Figure 2.2: Treatment of boundary cell using non-reflective boundary condition.

2.6.1 Non-reflective boundary condition

The plane wave analysis described in section 2.3.1, can be used also on a boundary with the normal pointing out of the domain. Since there are no cells outside the domain, some values $\vec{q}_b$ are prescribed to the boundary. Denoting the values in the cell adjacent to the boundary $\vec{q}_d$, the cell face values are calculated by $\vec{q}^A = 0.5\,(\vec{q}_b + \vec{q}_d)$. The situation is depicted in figure 2.2. Then, depending on the sign of the characteristic speeds, components from $\vec{q}^L = \vec{q}_d$ and/or $\vec{q}^R = \vec{q}_b$ are used to calculate the characteristic variables.

This method will absorb all plane waves approaching the boundary if they are aligned with the boundary normal. A wave which is not aligned with the boundary normal will, by this method, be misinterpreted as a plane wave, resulting in the wave being partially deflected.

2.6.2 Fixed static pressure

The non-reflective boundary condition is suitable for inlets, where values of all variables are known. But for outlet boundaries, all values cannot be specified since that would prevent a natural development of the flow in the domain. At least one variable, often the static pressure, must however be specified for the problem to be well posed. The simplest possible boundary condition is to use zeroth order extrapolation for all variables but the static pressure which is set to a fixed value. Such a boundary condition is totally reflective in terms of acoustic waves giving artificial pressure fluctuations of typical order $100\ Pa$. Hence, this simple method is not suitable for acoustic computations but accurate enough for most other computations.

Chapter 3

Other numerical methods

During this work, some development of the G3D code has been made. Section 3.1 describes the routines added for treatment of time dependent boundary conditions and the code has been rewritten in Fortran 90 which is discussed in section 3.2.

Correlations and fast Fourier transforms (FFTs) are important tools in the evalueation of the results. Some properties of these tools are discussed in sections 3.3 and 3.4

3.1 Inlet boundary treatment

For inlet boundary condition which have variations in space, the boundary data has to be interpolated to the computational grid in some way. For the method described here, the set of all points where data is given, must constitute a surface which is homeomorphic to an equidistant Cartesian grid. Data points with only two or three neighbors are considered edge points and points with four neighbors are interior points (see figure 3.1).

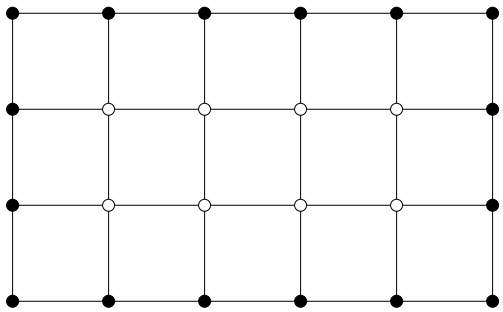

Figure 3.1: Boundary data set mapped onto an equidistant Cartesian grid. Filled circles: Edge points. Open circles: Interior points.

Each cell face on the boundary of the computational grid is treated separately. The coordinates for the cell face center, x_i^{CF}, are computed and compared to all interior points of the data set. A closest interior data point with coordinates x_i^{DP} will be found (see figure 3.2(a)). Since the data point is an interior point, it will have exactly four neighbor points which in turn will have enough neighbors to construct four surfaces, all having x_i^{DP} as one of their corners. This construction is depicted in figure 3.2(a). Each of these four surfaces are treated one by one, starting with for example the one up to the left in figure 3.2(a). The surface has corner coordinates x_i^1, x_i^2, x_i^3 and x_i^4 as shown in figure 3.2(b). A local coordinate system ξ, η is defined by the bilinear transformation

$$x_i^S = (1-\xi)(1-\eta)x_i^1 + \xi(1-\eta)x_i^2 + (1-\xi)\eta x_i^3 + \xi\eta x_i^4 \tag{3.1}$$

Thus, (ξ, η) has its origin in the lower left corner of the surface and (ξ, η) equals $(1, 1)$ in the upper right corner. With the constraints $0 \leq \xi \leq 1$ and $0 \leq \eta \leq 1$ a non-linear optimization routine, in this case Powell's method [16], is used to minimize the function

$$f(\xi, \eta) = \sqrt{\left(x_1^{CF} - x_1^S\right)^2 + \left(x_2^{CF} - x_2^S\right)^2 + \left(x_3^{CF} - x_3^S\right)^2} \tag{3.2}$$

For each surface, the value of $f(\xi, \eta)$ is the distance from CF to its projection on each surface, i.e. the length of the dotted arrows in figure 3.2(a). For one of the surfaces, $f(\xi, \eta)$ will be less or equal to $f(\xi, \eta)$ for all the other surfaces. Then the flux values assigned to the cell face, $\vec{q}^{\,CF}$ are computed by

$$\vec{q}^{\,CF} = (1-\xi)(1-\eta)\vec{q}^{\,1} + \xi(1-\eta)\vec{q}^{\,2} + (1-\xi)\eta\vec{q}^{\,3} + \xi\eta\vec{q}^{\,4} \tag{3.3}$$

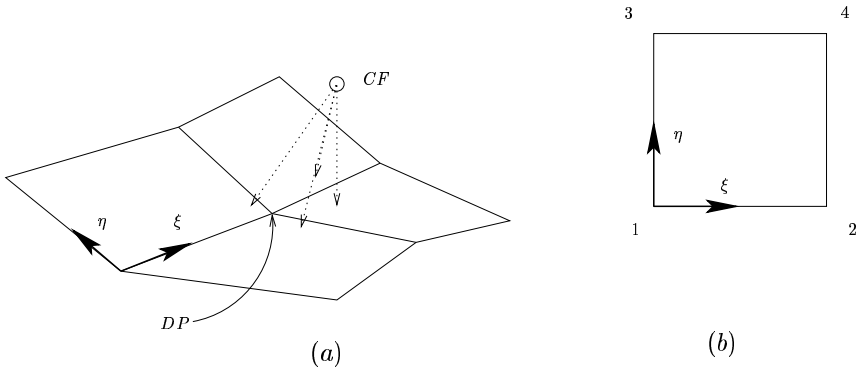

(a) (b)

Figure 3.2: (a): Projection of a cell face centrum (CF) on the surfaces spanned by the boundary data set. DP is the interior data point closest to CF. ξ and η are basis vectors for one surface. (b): One surface with corners 1, 2, 3 and 4.

using the ξ and η obtained from the optimization. $\vec{q}^{\,j}$ is the data in corner point j.

Since no integration procedure is adopted, the computational grid needs to be at least as fine as the data set. If the data set and the grid both happen to be Cartesian, this method is exactly equivalent to bilinear interpolation with zeroth order extrapolation if the data set does not cover the whole grid.

The method is quite fast. For a data set of 35×106 points and a grid with 120×64 cell faces, this method uses approximately one second to find interpolation coordinates for all cell faces.

3.2 G3D in Fortran 90

The code was orginially written in Fortran 77 using static allocation and COMMON areas for memory communication [10]. Such construction is sensitive to errors made by the user when defining the sizes of the common areas. The code, however was very modular in its construction making the code easy to rewrite in true modular form using Fortran 90 and thus getting access to dynamic allocation. Rewritten, the code, which operates using message-passing interface (MPI), only needs information how to distribute the blocks on the processors and the width of the widest discretization scheme.

The rewritten code was compared with the original version to confirm that they produced exactly the same result. Since allocation is a slow process, all allocation takes place in the beginning of the execution. The dynamic allocation, and also a broader memory structure, makes the Fortran 90 code little more than 20 % slower than the Fortran 77 version. This drawback can probably be eliminated since no effort was made to optimize the Fortran 90 code for speed.

The dynamic allocation is actually critical when designing post-processing codes and the modular structure of the computational code is convenient when reusing subroutines.

3.3 Correlations

Correlations is a statistical concept measuring the linear relation between two jointly distributed random variables [17]. In turbulence they are often used to measure scales of the flow, one variable taken as a velocity component at a fixed position in space and time and the other taken as a velocity separated from the first variable in space or time (or both).

If the separation is in time only, the *autocorrelation tensor* [18] is

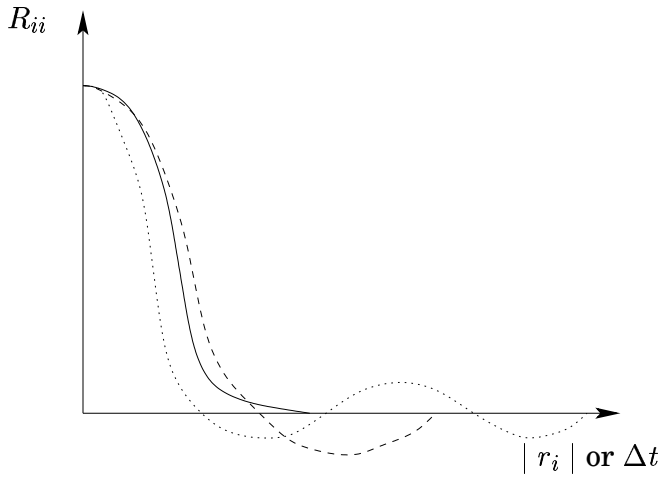

Figure 3.3: Hypothetical space or time correlations.

obtained by

$$R_{ij}(x_i, \Delta t) = \langle u_i'(x_i, t) u_j'(x_i, t + \Delta t) \rangle \tag{3.4}$$

A time scale characteristic for the energy-bearing scales, *the integral time scale*, is defined by

$$\tau(x_i) = \int_0^\infty \frac{R_{ii}(x, \Delta t)}{R_{ii}(x_i, 0)} \, d\Delta t \tag{3.5}$$

For stationary turbulent flows, normally only a single streamwise component, $R_{11}(x_i) = R_{uu}(x_i)$ is used.

The *two-point correlation tensor*, denoted $R_{ij}(x_i, r_i)$, is defined for points separated a distance r_i in space:

$$R_{ij}(x_i, r_i) = \langle u_i'(x_i, t) u_j'(x_i + r_i, t) \rangle \tag{3.6}$$

In analogy to the integral time scale, an *integral length scale*, ℓ, can be defined by

$$\ell(x_i) = \frac{3}{16} \int_0^\infty \frac{R_{ii}(x_i, r_i(s))}{R_{ii}(x_i, 0)} \, ds \tag{3.7}$$

where $3/16$ is a scale factor and s is a parametrization of the direction given by r_i such that $\mid r_i(0) \mid = 0$ and $\lim_{s \to 0} \mid r_i(s) \mid = \infty$.

As long as the correlations looks like the solid line in figure 3.3, a comparison between integral scales for different x_i makes perfect sense. If, however the turbulent structures consist of vortex-like structures, the correlations may look like the dashed line in figure 3.3, making comparison using integral scales ill defined. The correlation described by the dashed line obviously corresponds to a larger structure than the

correlation described by the solid line. Yet, an integral scale calculated using the dashed line will be much smaller than one calculated using the solid line. Attempts to define an unambiguous length scale include integration to the distance/time separation where the correlations first reach zero (see for example ref. [19]). Integration could also be performed using an absolute operator on the integrand. Whichever method that is choosen, there is always a risk that a method is chosen that gives the desired answer. Therefore, integral length scales will not be utilized in this work.

Correlations can also look as the dotted curve in figure 3.3. An physical explanation is that the flow has a periodicity corresponding to the separations between the peaks. Making an FFT of such a correlation will, in case of a two-point correlation, give the wave lenth of the repetition, while it for an autocorrelation, also called time correlation, gives the frequency at which the flow structures repeat them selfe.

3.4 FFT and power spectra

Very good descriptions of the theory on fast Fourier transforms (FFTs) can be found elsewhere [16]. Here only some aspects will be pointed out.

The data is assumed to be a time series $\{h(t_k)\}_{k=0}^{N-1} = \{h_k\}_{k=0}^{N-1}$ with N being an power of two. The function $h(t)$ is assumed to have a period $\Delta t N$ where Δt is the time interval between two samples. Neither may it contain frequencies higher than $1/(2\Delta t)$ (known as the Nyquist criterion). The discrete Fourier transform will contain frequencies

$$f_n = \frac{n}{N\Delta t} \text{ with } n = -\frac{N}{2}, \ldots, \frac{N}{2} \tag{3.8}$$

There is no standardized defenition of the discrete Fourier transform. For the one used in this work, the following relation is vaild between the transform and its inverse:

$$H_n = \sum_{k=0}^{N-1} h_k e^{2\pi i k n/N} \tag{3.9}$$

$$h_k = \frac{1}{N} \sum_{n=0}^{N-1} H_n e^{-2\pi i k n/N} \tag{3.10}$$

The discrete Fourier transform of $h(t)$ is then given by $H(f_n) = \Delta t H_n$. Observe that $H_{-n} = H_{N-n}$ follows from the periodicity of equation (3.9).

For the continous case, Parseval's theorem states that

$$\text{total power} = \int_{-\infty}^{\infty} \mid h(t) \mid^2 dt = \int_{-\infty}^{\infty} \mid H(f) \mid^2 df \tag{3.11}$$

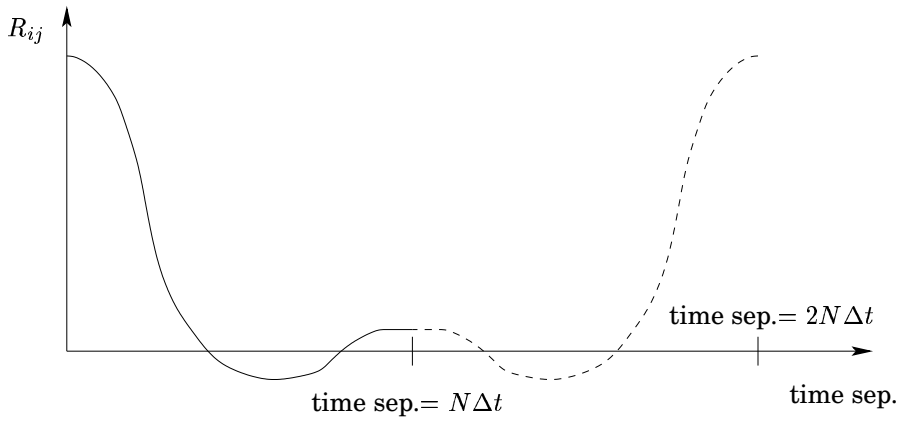

Figure 3.4: Extending an autocorrelation for Fourier transforming. Solid line: Actual correlation. Dashed line: Mirrored information.

When the power contained in the frequencies between f and $f + df$ is considered, no difference is made between positive and negative frequencies. Instead, a *power spectrum* $P_h(f) = \mid H(f) \mid^2 + \mid H(-f) \mid^2$ is defined. The discrete analog is dependent on the exact formulation of the transform. For a periodic time series the power spectrum will in this case be defined by

$$\begin{aligned} P_h(f_n) &= \frac{1}{N^2}\left(\mid H_n \mid^2 + \mid H_{-n} \mid^2\right) \text{ for } n > 0 \\ P_h(0) &= \frac{1}{N} \mid H_0 \mid \end{aligned} \tag{3.12}$$

It has the properties

$$\begin{aligned} P_h(0) &= \langle h(t) \rangle \\ \sqrt{\sum_{n>0} P_h(f_n)} &= rms(h(t)) \end{aligned} \tag{3.13}$$

where the rms is in turbulent sense, viz. deviation from the mean.

As mentioned in section 3.3, it is desirable to make FFTs of correlations. They do however not meet the requirement of periodicity. This can be circumvented by defining a sample series $\{h(t_k)\}_{k=0}^{N-1} \cup \{h(t_k)\}_{k=N-1}^{0}$ as illustrated in figure 3.4. That series is exactly periodic, but care must be taken when interpreting the result. The series $\{h(t_k)\}_{k=0}^{N-1}$ has N independent frequencies while $\{h(t_k)\}_{k=0}^{N-1} \cup \{h(t_k)\}_{k=N-1}^{0}$ will have $2N$ frequencies, but since no extra information has been added, only N of them will be independent. Also, the power spectrum will differ since R_{ij} already has unit power and must be kept

that way. Thus the power spectrum for a correlation is defined as:

$$\begin{aligned} P_h(f_n) &= \frac{1}{N}\left(\mid H_n \mid + \mid H_{-n} \mid\right) \text{ for } n \geq 0 \\ P_h(0) &= \frac{1}{N} \mid H_0 \mid \end{aligned} \tag{3.14}$$

Chapter 4

Computational setup

4.1 The domain

The computational domain is actually a numerical model of a part of an experimental test rig that is located at the department of energy technology, KTH. The experimental test section is $0.44\ m$ long, $0.10\ m$ wide and $0.12\ m$ high. At the bottom of the test section there is a bump. See reference [9] for more details about the rig. The computational domain consists of this test section, but it has been shortened $0.08\ m$ in the streamwise direction and translational periodicity was assumed in the spanwise direction for a width less than that of the test section. The width of the domain will be considered in chapter 5. Furthermore, the roof has been taken away and was replaced by a symmetry plane. A two-dimensional picture of the domain is shown in figure 4.1. To mimic the conditions in the test rig as far as possible, the symmetry line has been lowered by one momentum loss thickness based on the inlet boundary condition, so that $h = 0.1186154\ m$. In this way possible differences in mass displacement between measurements and calculations are prevented to a certain extent. The maximum height of the bump is $0.010477\ m$.

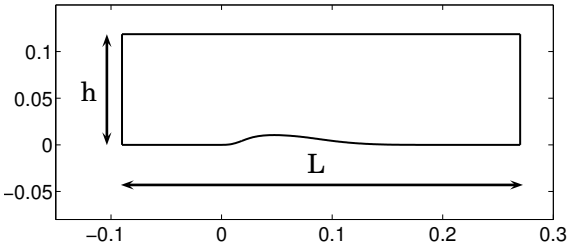

Figure 4.1: $2D$ projection of the computational domain.

The geometry is such that for some subsonic boundary conditions at the inlet and outlet, the flow will be accelerated over the bump and the sonic pocket that is formed will be terminated by a shock. Measurements have shown that no shock in the range of interest is so strong that it will reach up to the roof. Therefore, replacing the roof with a symmetry plane should not have any strong influence on the flow field.

4.2 Flow conditions

An LES simulation with all conditions set as in the experimental rig would, due to high computational costs, be more or less impossible. The Reynolds number based on $h/2$ and the free-stream inlet conditions would then be about 10^6. The number of nodes needed for such a case is far beyond our capacity today. Therefore the Reynolds number has been decreased by increasing the viscosity by a factor 11.25 up to $\mu = 1.8e^{-4} Pa\,s$. The boundary layer upstream of the shock is, of course, dependent on the Reynolds number. An effort to compensate for this was made by careful choice of inlet boundary conditions (see next subsection). However, it is thought to be better to carry out a well-resolved, accurate LES at a reduced Reynolds number, than an inaccurate LES at the original, high Reynolds number.

4.3 Boundary Conditions

As already mentioned, the upper boundary was set to be a symmetry boundary and the spanwise boundaries were given translational periodic boundary conditions. Along the wall, no-slip, adiabatic conditions were enforced.

From measurements [9] it is known that for free stream inlet boundary conditions of $M = 0.70$, $P_0 = 160.0\ k\,Pa$, $T_0 = 303\ K$ and for some outlet pressure there will be a shock at the back of the bump. In addition, the inlet should have a turbulent boundary layer. A boundary layer thickness of $8.95\ mm$ was given by a measurement made by Sigfrids [8], at the location $x = -0.10\ m$ whereas the computational inlet is at $x = -0.09\ m$ (see figure 4.1). Furthermore the measurement was made at a higher Reynolds number due to different viscosity.

An important aspect in the calculations is to match the experimentally obtained boundary layer thickness at the top of the bump, since it determines the acceleration of the flow. There are no simple tools for approximating the development of the boundary layer as it is accelerated over the bump. Instead, a theory for incompressible turbulent boundary layer [20], was used to calculate the expected boundary layer thickness at the start of the bump, $x = 0.0\ m$, in the test rig. Then, the

required δ_{99} at $x = -0.09\ m$ to get the same boundary layer thickness at $x = 0.0\ m$, but with the higher viscosity, was calculated. The calculations gave $\delta_{99} = 8.2\ mm$. Such a profile would have a Reynolds number $Re_\tau = 615$ based on u_* and δ_{99}.

A profile for incompressible flow measured by Johansson and Castillo [21] was used but needed rescaling. For a profile with a free stream velocity U_∞ the following relation is valid [22]:

$$\frac{U}{U_\infty} = f\left(\frac{xU_\infty}{\nu}, \frac{yU_\infty}{\nu}, *\right) \tag{4.1}$$

where f is some function describing the relation and $*$ denotes the dependence on upstream conditions. Rescaling Johansson's and Castillo's profile using this relation gave a profile with $\delta_{99} = 7.5\ mm$ and $Re_\tau = 632$. Both quantities are close to the desired values.

To get profiles for ρ and ρe_0, the temperature was assumed to followed the Walz' distribution [23]:

$$\frac{T}{T_\infty} = \frac{T_w}{T_\infty} + \frac{T_r - T_w}{T_\infty}\left(\frac{U}{U_\infty}\right) - r\frac{\gamma - 1}{2}M_\infty^2\left(\frac{U}{U_\infty}\right)^2 \tag{4.2}$$

where T_w is the wall temperature, T_r the recovery temperature and r the recovery factor. The expression

$$T_r = T_\infty + r\frac{U_\infty^2}{2c_p} = T_\infty\left(1 + r\frac{\gamma - 1}{2}M_\infty^2\right) \tag{4.3}$$

and the value 0.89 for r, were also taken from Schlichting [23]. As the wall was set to be adiabatic, $T_w = T_r$. The pressure was assumed constant through the boundary layer and its value was given by the measurements made by Sigfrids. Combined with the ideal gas law, the desired profiles were obtained.

The fluctuations were taken from incompressible DNS of fully developed channel flow. The data had to be rescaled based on u_*, ν and h_{DNS} versus δ_{99} where h_{DNS} was half the channel height for the DNS calculation. Observe that both space and time variables needed scaling. The pressure fluctuations were based on the dynamic pressure fluctuations from the DNS. Since the DNS was incompressible, the acoustic fluctuations were missing. They are however relatively small and were therefore neglected. Because fully developed channel flow has a much higher turbulent intensity in the middle of the channel than developing boundary layer has in the outer region, the fluctuations from the DNS had to be reduced. A filter was created by comparing RMS data from the DNS and the measurements made by Johansson and Castillo. The filter was applied to the fluctuations before they were added to the inlet profile. The resulting Reynolds stresses are displayed in figure 4.2.

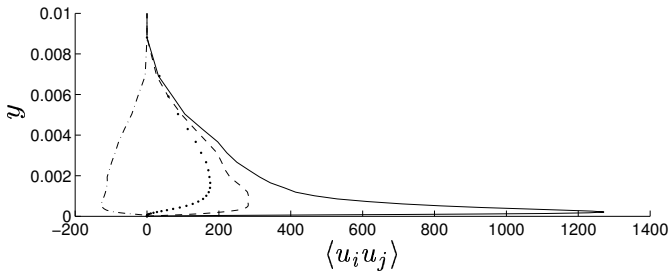

Figure 4.2: Reynolds stresses at the inlet. ——, $\langle uu \rangle$; · · ·, $\langle vv \rangle$; – – –, $\langle ww \rangle$; – · –·, $\langle uv \rangle$.

The mathematical form of the inlet boundary condition was that of a non-reflective boundary condition based on flow characteristics where $\rho, \rho u, \rho v, \rho w$ and ρe_0 are given as boundary values. The free stream value of these five were set to $1.3766\ kg/m^3$, $312\ Ns/m^3$, $0.0\ Ns/m^3$, $0.0\ Ns/m^3$ and $310\ kJ/m^3$.

In the experimental rig, the outlet pressure was used to control the strength and the position of the shock [9]. An outlet pressure of $114\ kPa$ gave a very weak shock at $x \approx 0.05$ while an outlet pressure of $104\ kPa$ gave a strong shock at $x \approx 0.07$. The measurements by Bron indicated that for an outlet pressure of $108\ kPa$, a maximum Mach number 1.3 was reached right before the shock. 1.3 is generally considered the critical Mach number to get separation for transonic flows with SWTBLI [2] and this was confirmed in Bron's experiments. The problem is that the flow in the wind tunnel features large zones of separation at the side walls, thus the flow is accelerated by 3D effects neither possible nor desirable to mimic in the computational domain. The best flow configuration, which was reached for $P_{out} = 103.5\ kPa$, was a shock at $x \approx 0.075$ and the maximum Mach number was 1.27 (see chapter 5). When the same shock strength was obtained in the test rig, the shock was positioned at $x \approx 0.065$. A stronger shock could have been achieved by lowering the outlet pressure even more, but that was not done since the shock then would have moved too close to the location where the wall curvature goes from convex to concave.

4.4 Data treatment

For each grid, a calculation was run until the average wall shear stress on the back of the bump showed no long time fluctuations. The calculations were then run for approximately 3 flow through times. During this time, 512 instantaneous solutions with equal time spacing were saved. Tests showed that second order statistics could be calculated from 300 samples only without loss of accuracy, but 512 were chosen because of

FFT calculations in the post processing.

As explained in the nomenclature, the code gives data in form of cell averages. For each node (node = grid node), the values of the adjacent cells were added and the sum divided by the number of adjacent cells. This makes the values of the interior nodes averages of eight cell values while the values assigned to a corner node equal those of its adjacent cell.

Depending on the application, the nodal data were then either averaged in the spanwise direction or interpolated onto the cells of another grid. Flow statistics such as Reynolds stresses were calculated from data averaged in both the spanwise direction and in time. For calculation of two-point correlations and frequencies, data have been interpolated to a sample grid and calculations carried out on this grid using the cell values. The results have then been averaged in the spanwise direction.

Chapter 5

Results

5.1 Grid studies

Resolution is always a critical issue and in this case also domain width since translational periodic boundary conditions are assumed in the spanwise direction. This section deals with those issues. Three grids are considered and are summarized in the following table.

Grid	**Nodes**	domain width
1	$261 \times 121 \times 65$	$0.0195\ m$
2	$306 \times 131 \times 86$	$0.0195\ m$
3	$306 \times 131 \times 171$	$0.0390\ m$

A first grid, *grid 1*, with $261 \times 121 \times 65$ nodes in the streamwise, wall-normal and spanwise direction respectively, was constructed covering a width of almost $0.02\ m$. The domain was chosen with this narrow width since much wider would have been too costly in terms of computational cost. The effect of the width will be considered later in this section. The maximum stretching of this grid was $11\ \%$.

Initial computations showed that the resolution in terms of Δx^+ and Δy^+ was satisfactory. On most locations Δy^+ for the first node was 0.5 and it was nowhere larger than 1. But there was a fairly large region where Δz^+ was more than 30 with a maximum value of almost 40. A well resolved LES should have $\Delta z^+ \approx 20$ with 40 as an absolute maximum [24]. Therefore, another grid with $306 \times 131 \times 86$ nodes spanning the same domain width was created. Motivation for the extra 45 nodes in the streamwise direction will be given later. A few nodes were added also in the wall normal direction to give a better stretching. Some pictures of this *grid 2* can be seen in figures 5.1, 5.2 and 5.3. In figure 5.1 the block decomposition of the grid is shown and figures 5.2 and 5.3 show close up pictures at the foot of the bump and at the shock foot position respectively. The grid is of course $3D$, but is homogeneous in the

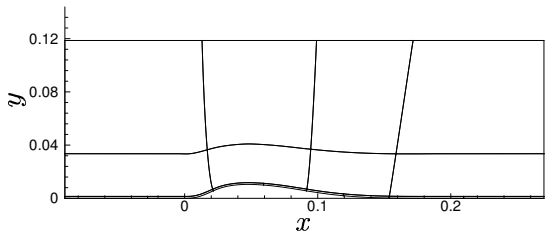

Figure 5.1: Block decomposition of grid 2.

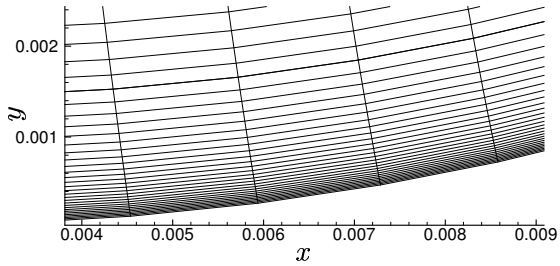

Figure 5.2: Close up of grid 2 at the foot of the bump.

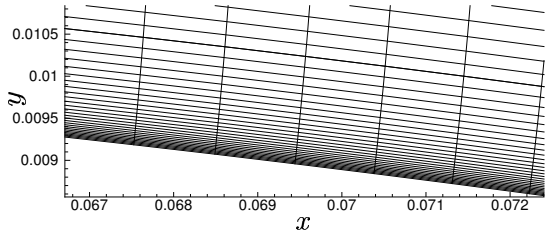

Figure 5.3: Close up of grid 2 at the shock foot position.

z-direction. Note that the x- and y-scales are approximately the same in figure 5.2 and 5.3.

To give an overview what the flow looks like, an average Mach contour plot is shown in figure 5.4. The maximum Mach number before the shock is 1.27. The results from grid 1 and grid 2 were compared. No differences could be seen in first order statistics and most second order statistics showed excellent agreement as can be seen in figure 5.5. Only in the $\langle ww \rangle$ Reynolds stresses, slight differences between the two computations can be seen (see figure 5.6). Notice that the streamwise scale is different in figures 5.5 and 5.6 and that the bump has been rescaled to have the same y-scale as the Reynolds stresses.

Another example of the near grid independence can be seen in figure 5.7 where the average wall shear stress can be seen. The negative wall shear stress on the bump indicates separation and that is confirmed by the large amplification of the Reynolds stresses seen in figure 5.5 and

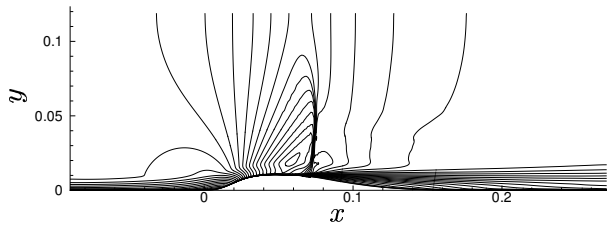

Figure 5.4: Average Mach contours computed on grid 2.

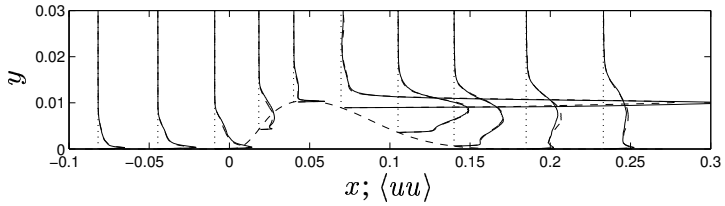

Figure 5.5: Comparison of the $\langle uu \rangle$ Reynolds stresses. —, grid 1; $--$, grid 2.

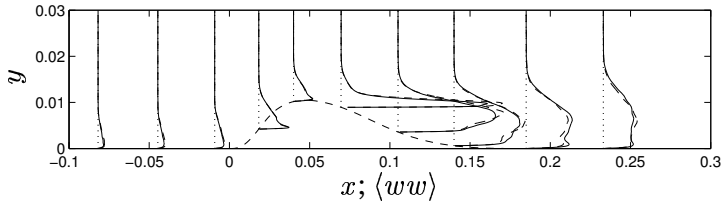

Figure 5.6: Comparison of the $\langle ww \rangle$ Reynolds stresses. —, grid 1; $--$, grid 2.

5.6. From the wall shear stress, the grid resolution in terms of inner variables has been calculated and Δx^+ and Δz^+ are shown in figures 5.8 and 5.9. They more or less only confirm what has already been said about the resolution.

Grid 2 has slightly more cells in the streamwise direction than grid 1. As can be seen in figure 5.8, they were used to get a generally better resolution, not only where Δx^+ were large, but also in the vicinity of the shock. The reason for the refinement in the shock region is that in the calculation on grid 1, almost no shock movement could be detected while in the experiments, the shock was clearly moving [9]. In this work shock movement was measured by FFT of the shock position outside the viscous region. Shock movement in experiments may very well be disturbances in the wind tunnel or unwanted $3D$-effects. But shock movement is often detected in computations of nominally $2D$ flows, especially in supersonic flows, so the grid was refined in the streamwise direction to make sure lack of shock movement was not caused by low resolution. Despite the refinement, no shock movement could be detected. This is

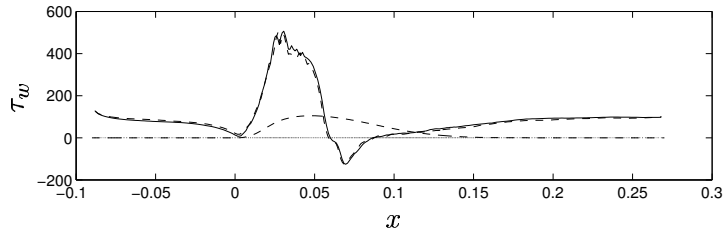

Figure 5.7: Comparison of wall shear stress. —, grid 1; −−, grid 2.

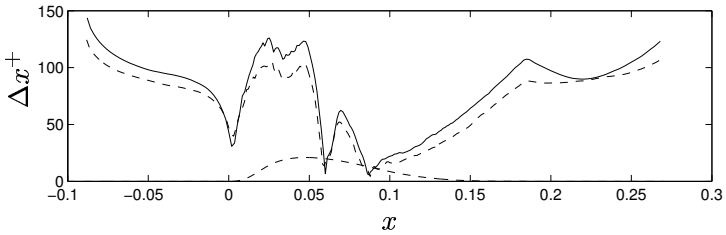

Figure 5.8: Comparison of streamwise resolutions. —, grid 1; −−, grid 2.

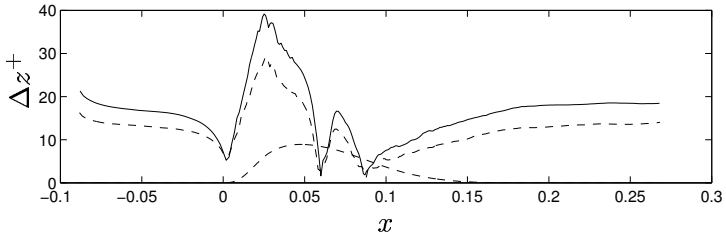

Figure 5.9: Comparison of spanwise resolutions. —, grid 1; −−, grid 2.

in disagreement with most experiments on transonic flows but in agreement with the results of Sandham et. al. [6]

As mentioned in chapter 2.3, it is important that the computational results are not too much dependent on the SGS model, i.e. the turbulent viscosity may at most be of the same order of magnitude as the kinematic viscosity. The maximum value of ν_t/ν found in the 512 samples was 0.39. This low number confirms that the solution is only weakly dependent on the SGS model. Thereby, it cannot be stated that the subgrid model is good enough. Looking at figure 5.7, a plateau can be seen in τ_w before it reaches its minimum value. Compared to other experiments, a more typical configuration is a local minimum before the global minimum indicating preseparation before the large, strongly separated, region. This preseparation is connected to a lambda-shock formation present at high enough Mach number before the shock. Garnier et. al. [7] made LES calculations of supersonic SWTBLI using higher Reynolds number and a more advanced subgrid model. Their results showed that if the SGS model was turned off, the preseparation, oth-

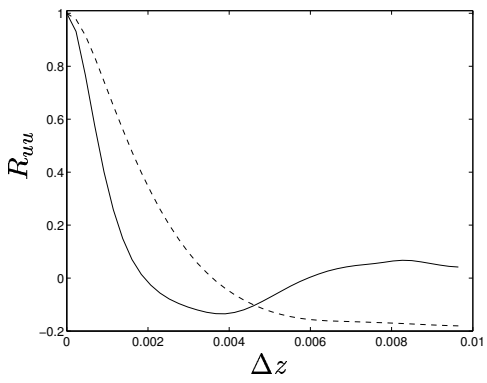

Figure 5.10: Two-point correlations for grid 2. ——— , taken before the bump at $x = -0.0155,\ y = 0.00125$; $- - -$, taken down stream of the shock at $x = 0.1155,\ y = 0.0076$.

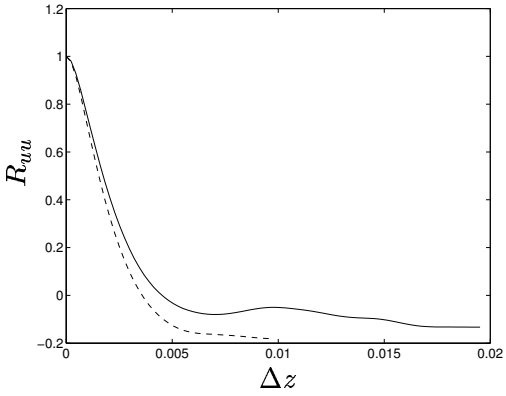

Figure 5.11: Comparison between two-point correlation for grid 2 and for grid 3 both taken at $x = 0.1155, y = 0.0076$; ——— , grid 3; $- - -$ grid 2.

erwise present, disappeared. It is possible that the SGS model used here is too simple to be able to capture the correct wall shear stress distribution. A much more probable explanation, however, is that the low Reynolds number has increased the interaction length, hindering preseparation.

From the small deviations in the Reynolds stresses and other statistical quantities, the good values of Δx^+, Δy^+ and Δz^+ and the low ν_t/ν, the only conclusion possible was that at least grid 2 has enough resolution for LES of this flow.

The important issue of domain width was investigated with two-point correlations in the spanwise direction. For a domain to be wide enough, the two-point correlations must have vanished at a separation of half the domain width. Two-point correlations are often normalized by their auto-correlations and care must be taken so that the auto-correlations are not small compared to the maximum normal Reynolds stresses. Therefore, two-point correlations were calculated for several wall normal distances and only correlations strong enough were used in the analysis. Plotting two-point correlations for several streamwise positions showed that the domain was wide enough to contain the largest spanwise structures of the boundary layer before the shock, but a bit downstream of the shock, the larger structures were exactly half the domain wide, which shows that the domain width was not sufficient. Figure 5.10 shows two typical correlation curves, one on the flat plate

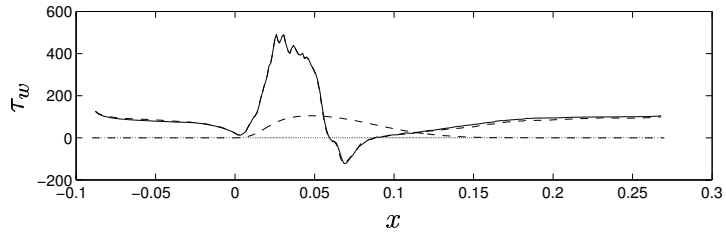

Figure 5.12: Comparison of the wall shear stresses. —, grid 3; −−, grid 2.

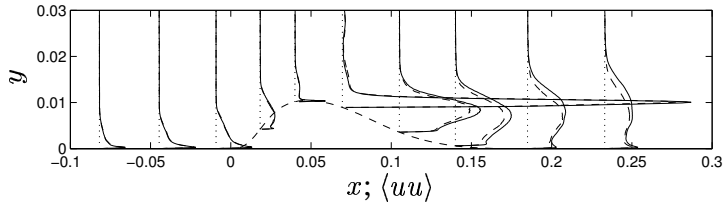

Figure 5.13: Comparison of the $\langle uu \rangle$ Reynolds stresses. —, grid 3; −−, grid 2.

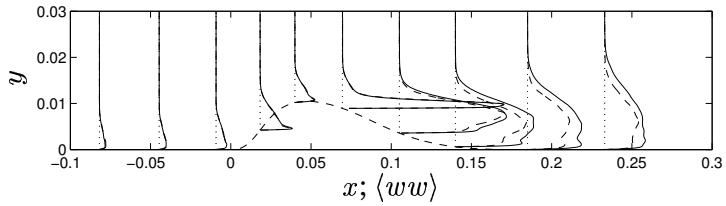

Figure 5.14: Comparison of the $\langle ww \rangle$ Reynolds stresses. —, grid 3; −−, grid 2.

before the bump and one some distance behind the shock.

To meet the requirements of larger domain width, a *grid 3* was created. It had the same resolution as the *grid 2*, but with twice the domain width, i.e. approximately $0.04\ m$ instead of $0.02\ m$. In figure 5.11, one of the two-point correlations from figure 5.10, the dashed line, is compared to the corresponding two-point correlation computed from the results for grid 3. Apart from the somewhat strange behavior for large Δz, which will be treated in the next section, the correlation for grid 3 is satisfactory. Although only one example is shown in figure 5.11, it displays the general trend for the spanwise two-point correlations. For first order statistics, both primary data, such as velocity and wall pressure, and gradients did not changed notably by the widening of the domain. Example of this can be seen in figure 5.12 where the wall shear stresses are compared. The Reynolds stresses, on the other hand, showed deviations which at most were somewhat less than 50 %. The $\langle uu \rangle$ and $\langle ww \rangle$ Reynolds stresses are shown in figures 5.13 and 5.14 respectively. 50 % deviation can sound like much, but it is partly an artifact of normal-

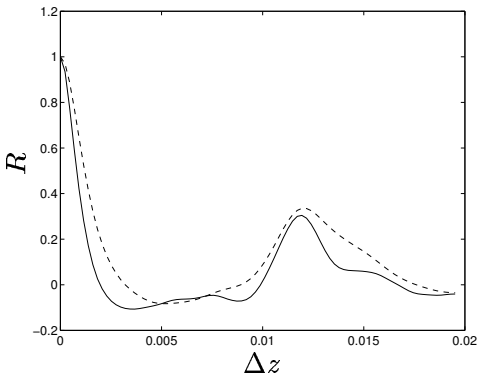

Figure 5.15: Two-point correlations at $x = -0.0145\ m$, $y = 0.00125\ m$. ——, R_{uu}; − − −, R_{ww}.

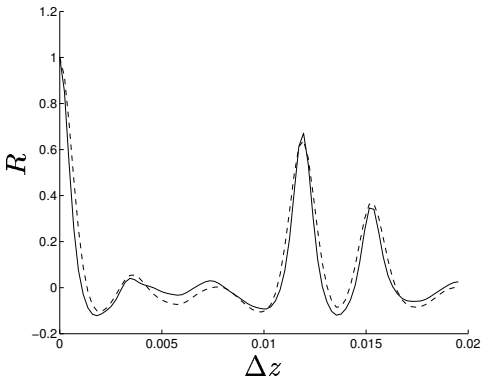

Figure 5.16: Two-point correlations at $x = -0.0891\ m$, $y = 0.273\ mm$; ——, R_{uu}; − − −, R_{ww}.

ization. For example, $\max(\Delta\langle uu\rangle)/\max(\langle uu\rangle)$ is not more than $14\ \%$, so the absolute values of the deviations are large, but, taking into account also the two-point correlations and very good agreement in first order statistics, not large enough to justify calculations on a grid even wider than grid 3.

5.2 Flow studies

All results discussed in this section are taken from computations performed on grid 3 since it is the only grid with both good enough resolution and wide enough domain.

It must always be checked, that the flow created in a simulation, really is the flow that is supposed to be studied. There are two major points of concerns in this computation. One is the strange behavior of the two-point correlations at large spanwise separations, the other that the shock is not moving.

5.2.1 Spanwise structures

Before proceeding with the analysis of the two-point correlations, it should be mentioned that it takes very large amount of data to get those correlations to converge, especially for large separations. As can be seen in for example figure 5.11, the correlation for grid 3 exhibits oscillations that can be caused by too few data samples. Depictured in figure 5.15, are the $\langle uu\rangle$ and the $\langle ww\rangle$ two-point correlations at $x = -0.0145\ m$, $y = 0.00125\ m$. At a beginning, they fall off as expected, but the rela-

tively high correlations at $\Delta z \approx 0.0012\ m$ are not expected. They turn out to originate from the inlet boundary conditions. Figure 5.16 shows the same correlations at the inlet ($x = -0.0891\ m$, $y = 0.273\ mm$) and both have sharp peaks at $\Delta z = 0.0119\ m$ and $\Delta z = 0.0153\ m$ and some smaller oscillatory peaks. As mentioned in section 4.3, fluctuations from DNS data were added to a measured velocity profile, but the DNS data covered only a width of $1.2\ cm$. To cover all of the computational domain, the turbulent data was repeated until the whole domain was covered. This procedure is the cause of the peaks at $\Delta z = 1.2\ cm$. The other peaks are also due to the same procedure, but they turn up at other Δz because the domain is covered by 3.28 repetitions of the DNS data, not an integer number.

It was clear from the beginning that the two-point correlations would look like this directly after the inlet, but it was not expected that the peaks would persist that far downstream of the inlet. Even after the flow has accelerated up the bump, the $\langle ww \rangle$ correlation shows a peak at $\Delta z \approx 1.3\ cm$. The turbulent structures on the inlet are repeated each $1.2\ cm$, but since all two-point correlations goes to zero within a separation shorter than $0.6\ cm$, these structures are independent of each other. Thus, the peaks are pure artifacts of the construction of inlet boundary condition. Because the inlet structures are fully physical to their nature, we consider the computations to be valid. The only problem is that the spanwise two-point correlations cannot be used to draw any further conclusions regarding the size of the turbulent scales. Remedy for this problem will be discussed in chapter 6.

5.2.2 Shock movement

The issue of shock movement requires detailed flow analysis. That there really is no shock movement could be seen both from FFT of the shock position and from animations of the flow field. If an FFT is made of the shock position and the power spectrum is plotted as a function of the frequency, only one sharp peak at $f = 0\ Hz$ with $P_h(f = 0) = 0.07$ (the mean shock position) is visible, the amplitude on every else frequency being at least a hundred times smaller. The little movement there is, can be analyzed by studying the the power spectrum of $x_{shock} - \langle x_{shock} \rangle$ which is shown in figure 5.17 for $y = 0.025\ m$. There are some low frequency shock movements, but as can bee seen from the scale of the power spectrum, they are of very low amplitude, making them unqualified as large scale shock movement.

It is not clear in exactly what frequency region to expect shock oscillations. Measurements by Bron [9] show that the shock frequency is very low, mostly contained in the region $0 - 100\ Hz$ with an additional single peak at $350\ Hz$. It is possible that the simulation length of $5\ ms$

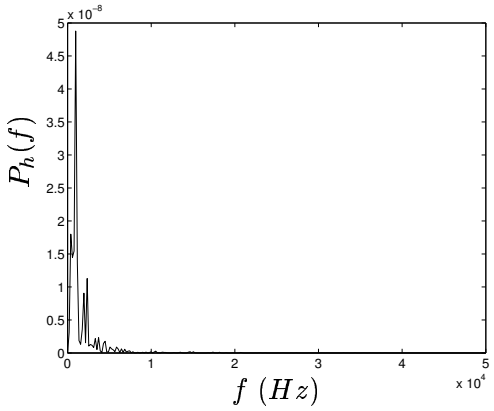

Figure 5.17: Power spectrum of $x_{shock} - \langle x_{shock} \rangle$.

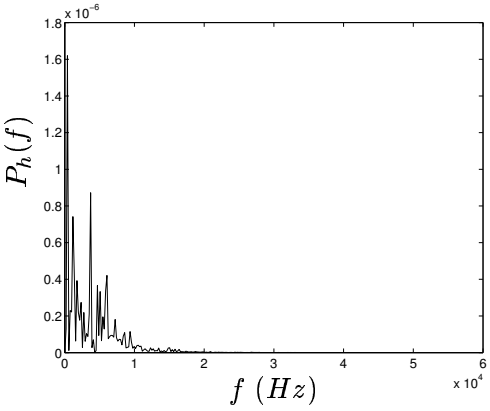

Figure 5.18: Power spectrum of upstream traveling sound waves at $x = 0.16\ m$ and $y = 0.05\ m$.

is too short to resolve shock oscillations, but in the measurements made by Bron, the shock was moving over a $\Delta x \approx 1\ cm$, and during the $5\ ms$ simulated here, the shock is absolutely stable. If the largest amplitude was connected to a frequency of for example $100\ Hz$, at least half a revolution would have been visible, resulting in the shock traveling a total of $1\ cm$. That leaves only three possible explanations. One is that the large scale shock movements have frequencies in order of $10\ Hz$, but that is much slower than any other characteristic time scale in the flow, especially those considered as candidates for shock movement, for example the separation bubble and the incoming boundary layer, leading to the second possible explanation: The large scale shock movements in the experiments may be due to disturbances in the wind tunnel facility. The last possible explanation is that the modified viscosity has altered the flow field and thereby eliminate shock movement. The truth of such a statement cannot be examined using the current results, but the results can be used to rule out possible explanations of shock movement.

It is a bit dangerous to use such simple outlet boundary condition as constant static pressure. Most computations performed today use buffer zones to prevent reflections at the outlet, reflections that result in artificial sound waves traveling upstream. If such artificial reflections reach the chock, they might interact with it causing unphysical shock movement, or, which can be suspected in this case, prevent shock movement. To analyze the information brought to and transported from the shock, the plane wave analysis used to compute the convective fluxes (see section 2.3.1) was applied before and after the shock. In particular, the

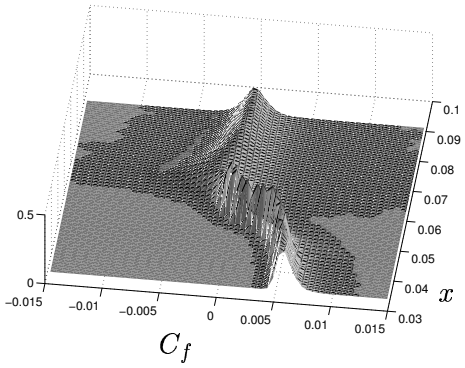

Figure 5.19: $3D$ visualization of the PDF of C_f.

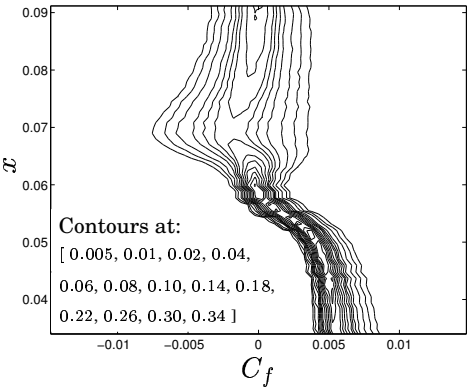

Figure 5.20: Contour lines of the PDF of C_f

power spectrum of the upstream traveling waves, i.e. those possibly emanating from the outlet, taken at $x = 0.16\ m$ and $y = 0.05\ m$ is shown in figure 5.18. In this case, the unit of P_h is density squared and corresponds to pressure fluctuations of magnitude a few hundred Pascal. The only way these waves can prevent shock movement, is if some of their frequencies are resonance frequencies of the shock *and* that they have exactly the opposite phase of whatever physical phenomena that would have produced shock movement if the artificial sound waves were not present. The risk that this is the situation is negligibly small, but can be excluded completely only if a buffer region is introduced.

5.2.3 The separated region

Shock oscillation seems at least partly to be connected to possible separation of the boundary layer with only small oscillations if there is no, or weak, separation [9]. The concept of incipient separation and its detection is thoroughly treated in reference [2]. Incipient separation is when the averaged τ_w is everywhere positive except for one point where it equals zero. As can be seen in figure 5.12, the flow field considered here is well beyond incipient separation. For the flow to be effectively separated, there has to be a sizable region where the probability for back-flow is larger than 0.5. In figures 5.19 and 5.20, the probability density function, PDF, of the skin friction coefficient, C_f, is given as a function of the streamwise position x. The distribution includes instantaneous data from all spanwise positions. As can be seen, the presence of the shock is first felt by the fluid at $x \approx 0.045m$ resulting in a decrease in C_f, but the variance of the distribution of C_f is not changed until the

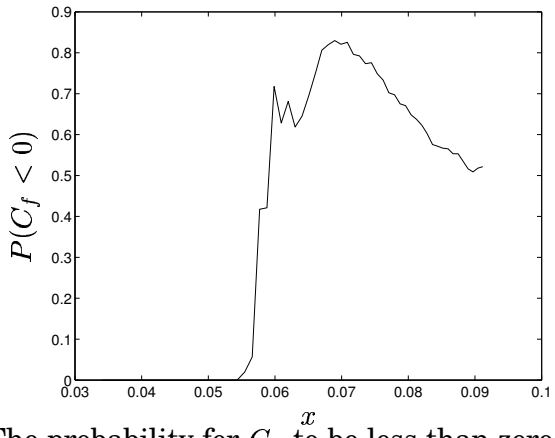

Figure 5.21: The probability for C_f to be less than zero as a function of streamwise position.

fluid reaches $x \approx 0.06\ m$ where the variance increases drastically, indicating effective separation with high intermittency. The probability for back flow can be found by integrating the PDF for all negative C_f, the result is shown in figure 5.21. Clearly, there is a separated region, $P(C_f < 0) > 0.5$, of 3 cm ranging from $x \approx 0.06\ m$ to $x \approx 0.09\ m$.

Three centimeters is in this case a rather large length scale, yet, it is not clear that the separated region can be considered sizable. Figure 5.22 depicts streamlines calculated from the average solution and as can be seen, the separation bubble is merely one millimeter high. On the other hand, visualizations of the instantaneous flow field reveal a different picture. An example is shown in figure 5.23. It is obvious that in the separated region, the mean flow field bears little resemblance to the real flow structures which are not anywhere stationary and several millimeters high. Thus, the seemingly low height of the separation region, is because there are several recirculation bubbles which are not stationary. In other words, if the flow is studied using first order statistics, the separation is concealed by the large Reynolds stresses.

There is no unambiguous method for calculating the size of the largest turbulent structures. As already discussed, the spanwise two-point correlations cannot be used. Turning to the uu time correlation, structures like the ones shown in figure 5.23 can be argued, using the concept of frozen turbulence, to give negative contributions to the time correlations. That makes the ordinary interpretation of the integral time scale questionable. Some representative time correlations for $x = 0.05\ cm$, $x = 0.06\ cm$ and $x = 0.07\ cm$ are shown in figures 5.24 and 5.25, all taken roughly half a millimeter from the surface. The downstream part of the separation bubbles are probably responsible for the negative cor-

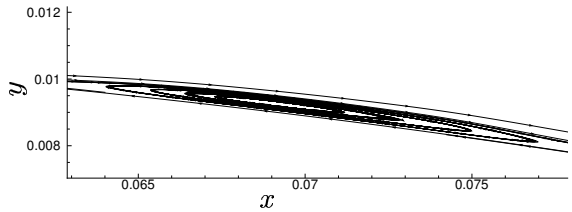

Figure 5.22: Streamline calculated from the averaged flow field.

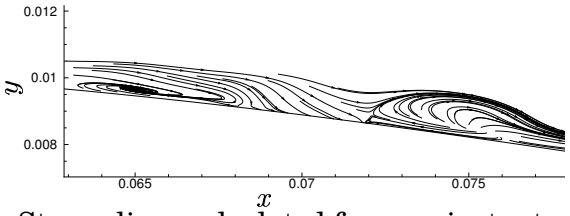

Figure 5.23: Streamlines calculated from an instantaneous flow field.

relations in the range $0.14 \cdot 10^{-4} < \Delta t < 0.5 \cdot 10^{-4}$ s, but they cannot explain the oscillatory trends in the correlations. These oscillations could be due to bad convergence or repeating turbulent structures. Whichever is the case, just by looking at the correlations, it is clear that the time scale increases by approximately a factor three as the flow separates.

The extreme values of the Reynolds stresses are shown in figure 5.26, where it can be seen that $\sqrt{\langle uu \rangle}/U_\infty$ increases by more than 300 % as the fluid passes through the interaction region. According to reference [2], such large amplification in $\sqrt{\langle uu \rangle}/U_\infty$ indicates strong separation. Also visible is the high degree of anisotropy after the shock which is to be expected since the shock is a most inhomogeneous phenomenon [25]. In figure 5.27 the distance to the wall for the maxima of the Reynolds stresses are shown. The maximum positions moves towards the wall as the boundary layer is retarded by the adverse pressure gradient. As the fluid passes through the separation region, turbulence is thrown out from the wall where it creates a strong turbulent region, possibly a vortex sheat. This region is clearly visible in figures 5.13 and 5.14.

Most statistical limits for separation, like increase in Reyolds stresses, do not take into account the curvature of the wall and the concept of effective separation is a bit vague. The important point here is that the flow features strong, unsteady structures under the shock, structures that could be the source for shock movement. The PDF of C_f, and the comparison between the average and instantaneous streamlines show that there is separation and that the flow field is highly unsteady. The structures are furthermore strong in the sense that the

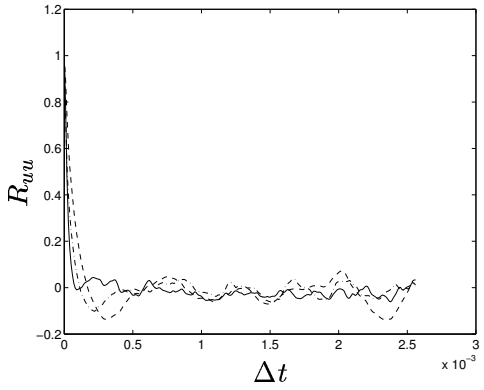

Figure 5.24: Time correlations for $x = 0.05\ m$ (——), $x = 0.06\ m$ (– – –) and $x = 0.07\ m$ (– · –·)

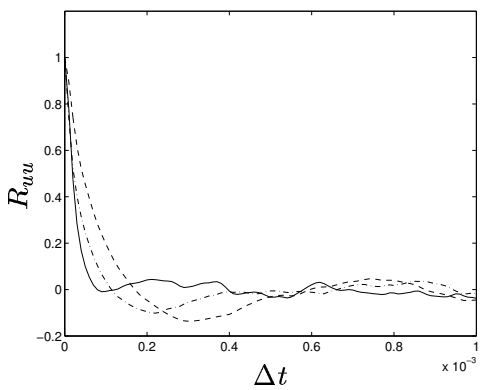

Figure 5.25: Closeup of figure 5.24 for $0 \leq \Delta t \leq 1 \cdot 10^{-3}\ s$.

Reynolds stresses are amplified with several hundred percents.

For supersonic flow in a compression ramp formation, Thomas et. al. [26] related the shock movement to the frequency of the separated region. There are significant differences between the current case and the supersonic one. In the supersonic case, the separation bubble is

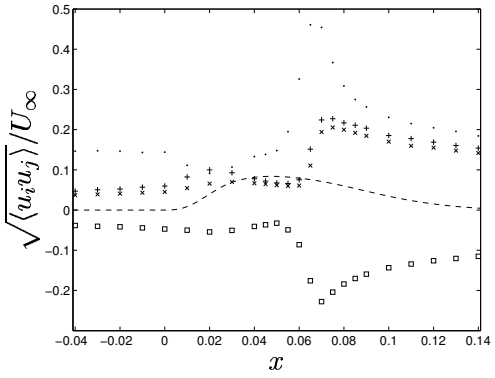

Figure 5.26: Normalized maximum values of the Reynolds stresses. $\cdot = \sqrt{\langle uu \rangle}/U_\infty$; $\times = \sqrt{\langle vv \rangle}/U_\infty$; $+ = \sqrt{\langle ww \rangle}/U_\infty$; $\square = \sqrt{\langle \mid uv \mid \rangle}/U_\infty$(sign restored). $---$ is the wall profile.

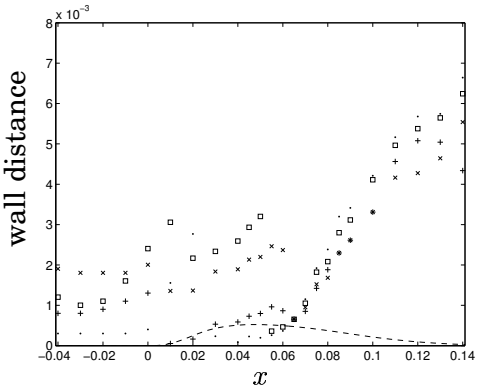

Figure 5.27: Distance from wall for the maxima of the Reynolds stresses. $\cdot = \sqrt{\langle uu \rangle}/U_\infty$; $\times = \sqrt{\langle vv \rangle}/U_\infty$; $+ = \sqrt{\langle ww \rangle}/U_\infty$; $\square = \sqrt{\langle \mid uv \mid \rangle}/U_\infty$. $---$ is the wall profile.

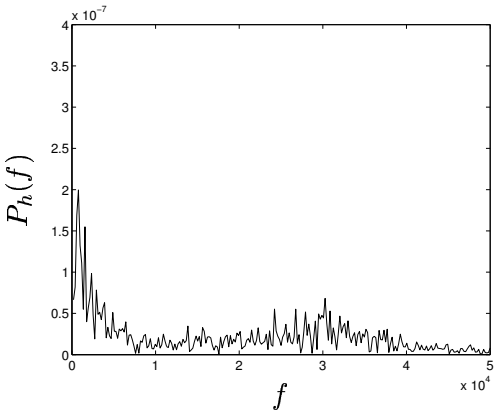

Figure 5.28: Power spectrum of the fluctuations of C_f at $x = 0.06\ m$.

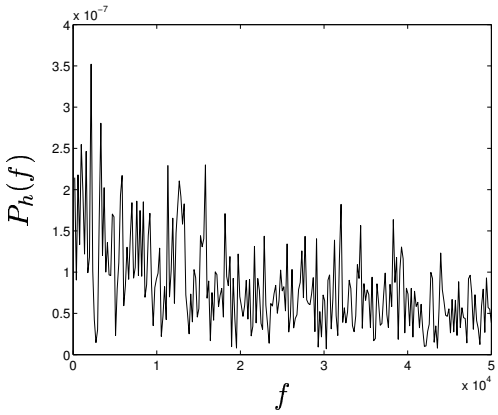

Figure 5.29: Power spectrum of the fluctuations of C_f at $x = 0.07\ m$.

'trapped' between the shock and the compression ramp, whereas the current flow features not one, but several, separation bubbles. Thus, no single turn-over time can be computed for the current case. Instead spectra based on the fluctuations of C_f were computed from $x = 0.06\ m$ and $x = 0.07\ m$ and averaged in the spanwise direction. The results are shown in figures 5.28 and 5.29. In the beginning of the separation, at $x = 0.06\ m$, the fluctuations are mostly of frequencies in the region $500 < f < 3000Hz$, but also some fluctuations can be found in a broad spectra around $f = 31\ kHz$. Further downstream, at $x = 0.07\ m$, the fluctuations are stronger and all frequencies are represented.

If it is assumed that the oscillations of the correlations in figure 5.24 represent recurrent flow structures, then the corresponding power spectrum will feature peaks at the frequency of this recurrence. The power spectra are shown in figures 5.30 and 5.31. At the start of the separation, $x = 0.06\ m$, structures of frequencies around $1500\ Hz$ dominate, but at $x = 0.07\ m$, the frequency content is broadened with $f \approx 2300\ Hz$ being the strongest frequency. From visualizations, the most conspicuous recurrence is that of large separation bubbles which form close to the surface and are ejected out in the free stream. At this ejection, several large scale structures are formed and it is very possible that the low frequencies in figures 5.30 and 5.31 originate from this process.

In conclusion, the strongly separated region features more or less all frequencies, some more important than other, but non of them triggers shock movement.

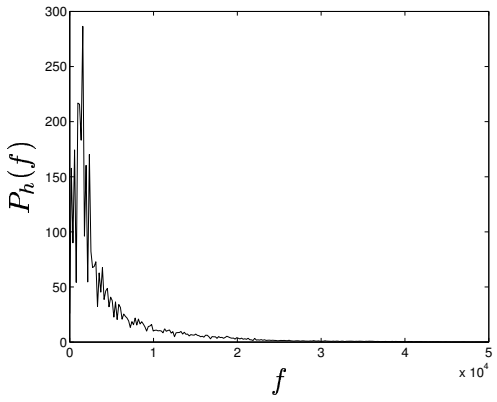

Figure 5.30: Power spectrum of time correlation $R_{uu}(\Delta t)$ at $x = 0.06\ m$.

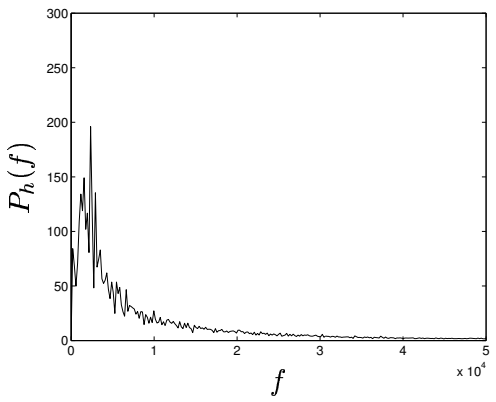

Figure 5.31: Power spectrum of time correlation $R_{uu}(\Delta t)$ at $x = 0.07\ m$.

5.2.4 The incoming boundary layer

Reason for the unorthodox properties of the separated region can be sought in the boundary layer approaching the shock, the so called incoming boundary layer. Also, several investigations of supersonic compression ramp flow have pointed out the burst frequency in the incoming boundary layer as the frequency of the shock movement. See for example reference [27] and [28].

The boundary layer was designed to have correct turbulent intensity at the inlet and to match the thickness of the experimental boundary layer at the bump foot. However, as the flow is accelerated up the bump, it is influenced by a favorable pressure gradient which starts a relaminarization process, a process which rate is proportional to the viscosity. Reference [29] describes the acceleration parameter

$$K = \frac{\nu}{U_\infty^2} \frac{\partial U_\infty}{\partial s} \tag{5.1}$$

where $\partial/\partial s$ represents derivation in the streamwise direction. For relaminarization to occur, K should be larger than $3 \cdot 10^{-6}$ over a long enough streamwise distance. For this computation K reaches above that limit, but as can be seen in figure 5.26, the boundary layer stays turbulent for all x. This however indicates that the viscosity could not have been much higher.

An effect of the far proceeded relaminarization process is that the form factor of the boundary layer is affected. Lower Reynolds number gives lower form factor as the flow is accelerated. Reference [2] also states that the strength of the separation is dependent on the form

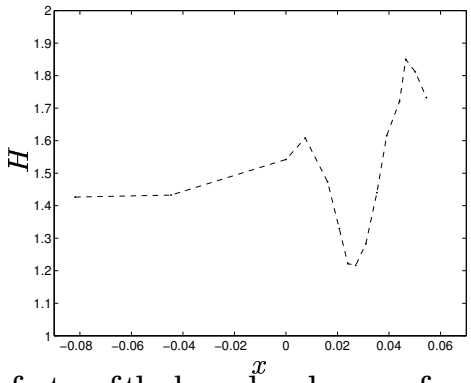

Figure 5.32: Form factor of the boundary layer as function of streamwise position x.

factor but independent of the Reynolds number with separation if the shock is strong enough to force H to become larger than 2.6, the exact number depending on the curvature of the wall. This number is close to 2.7 which was obtained as a separation criterion by Castillo et. al. [30] in their similarity analysis of incompressible equilibrium boundary layers. The incoming boundary layer is probably not an equilibrium boundary layer, but neither are those in reference [2]. The form factor for the current case is plotted as a function of x in figure 5.32. It is never anywhere near 2.6, yet strong separation do occur and the curvature of the wall is not strong enough to explain this large deviation in maximum form factor from the conventional value. Obviously, it is not necessary for the form factor to reach 2.6 for separation to occur.

To detect possible burst events in the incoming boundary layer of the current case, an indicator function was applied a distance $0.5\delta_{99}$ from the wall at $x = 0.05\ m$. The indicator function, I_M, was defined by

$$I_M = \begin{cases} 1 & \text{if } M > \langle M \rangle + \sigma_M \\ -1 & \text{if } M < \langle M \rangle - \sigma_M \\ 0 & \text{otherwise} \end{cases} \tag{5.2}$$

where σ_m is one standard deviation of the Mach number distribution in the point where I_M is measured. This is the same indicator function that was applied by Wu and Martin [28]. They found that bursts and shock movement had a main frequency of $0.14U_\infty/\delta$ which in this case would be approximately $0.14 \cdot 330/0.008 = 5.8\ kHz$. The result is displayed in figure 5.33. There is one peak in the region of interest, but it is not very strong. Ichimiya et. al. [31] describe the effect of a relaminarization process on the bursting frequency. Their conclusions were that the relaminarization starts from the outer layer and that the bursting

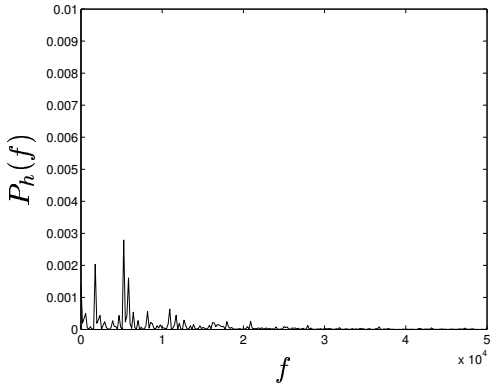

Figure 5.33: Power spectrum of the indicator function I_M taken at $x = 0.05\ m$ and $y = 0.014\ m$.

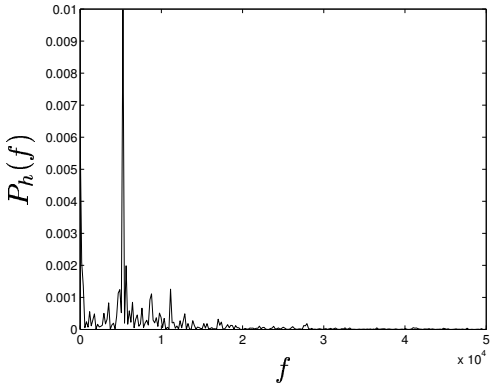

Figure 5.34: Power spectrum of the indicator function I_M taken at $x = 0.05\ m$ and $y = 0.012\ m$.

frequency decreases, at least in outer scaling. For comparison, the indicator function was applied at the same x but at a distance $0.25\delta_{99}$ from the wall. The resulting power spectrum is shown in figure 5.34. Here a sharp peak at $f = 5.3\ kHz$ which probably is the sought-after bursting frequency. That it is much stronger a bit closer to the wall than in the supersonic case is in agreement with the results of Ichimiya et. al. Of course the bursting frequency cannot be found in the shock movement since there is non, but more surprisingly; it cannot be found in the separated region either.

In figure 5.33 there is yet another peak which is in the same region as the important frequencies in the separated region. To get a more complete picture, power spectra of the skin friction coefficient and of the time correlation, both computed for $x = 0.05\ m$, are shown in figures 5.35 and 5.36. Both can be seen to have peaks at very low frequencies, both probably emanating from the same boundary layer phenomena, uncertain which. But the power spectrum of the time correlation contains much more information. Apart from the lowest peak, three more peaks can be found. The approximate location for these peaks are $3200\ Hz$, $5000\ Hz$ and $8200\ Hz$. There is actually a peak also at $1550\ Hz$. Both $1550\ Hz$ and $3200\ Hz$ can be found in the separated region (see figure 5.31) and $5000\ Hz$ is very close to the bursting frequency. This last observation strengthen the hypothesis that the oscillations in the time correlation really originates from flow structures. The lowfrequency peak in figure 5.33 at $1700\ Hz$ and the peak at $1550\ Hz$ in the power spectrum of the time correlation could much well be connected to the same recurrent phenomenon, a phenomenon which gives rise to a

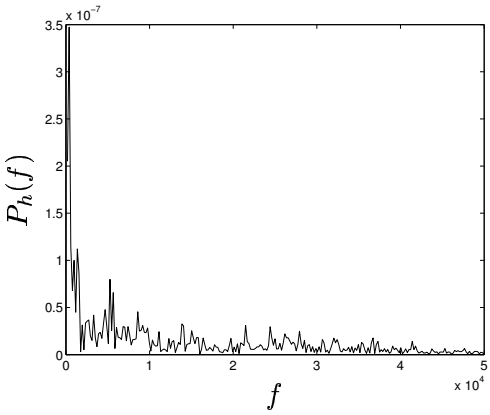

Figure 5.35: Power spectrum of the fluctuations of C_f at $x = 0.05\ m$.

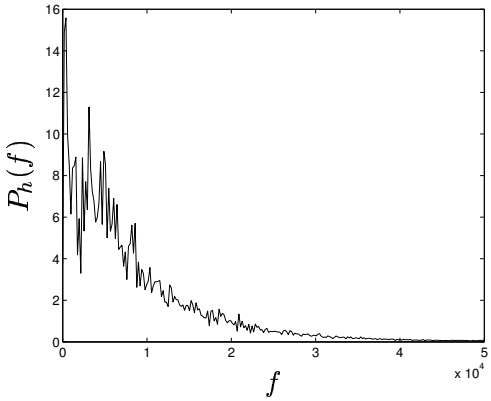

Figure 5.36: Power spectrum of the time correlation R_{uu} at $x = 0.05\ m$ shown in figure 5.24.

burstlike event in the outer parts of the boundary layer.

It is clear that the SWTBLI picks one or several frequencies from the incoming boundary layer and creates structures of these frequencies. These frequencies ssems to correspond mainly to repetition of flow strucutures in the incomming boundary layer.

Chapter 6

Conclusions

The calculation presented here of a transonic SWTBLI is accurate with good resolution, wide enough domain and little dependence on the subgrid model. It could however be improved on three points

- A more advanced subgrid model could be used, or at least variable filter width introduced.
- Buffer zone, or absorbing boundary condition, could be added at the outlet.
- Different treatment of the inlet data.

The first two points are computationally costly, but not impossible to attend to. The last problem is of a more cunning nature. The only way to extend the DNS data is to repeat it, which is in accordance with its own boundary conditions. Unless the DNS is made as wide as the LES domain, it is impossible to get rid of the peak turning up where the DNS data is repeated. Some of the smaller peaks could though be deleted by having an LES domain that is an integer multiple of the DNS channel. But if there are resources to run a wide enought DNS to acquire turbulent inlet data, it is highly recommended to do so.

The flow is strongly separated in terms of probability for back-flow and increase in time-scales and Reynolds stresses through the interaction region. The separated region features high intermittency with several frequencies, but non of the triggers shock movement. In fact, the shock is quite still which is in contradiction to measurements of the flow. At least, that situation removes the theory that the separated structures alone should trigger shock movement.

The incoming boundary layer is on the brink of relaminarization, but stays turbulent everywhere. The high viscosity makes the form factor of the incoming boundary layer very low and it never reaches the conventional 2.6 before separation. This suggests that the separation strength

is not independent on Reynolds number as suggested in reference [2] and that a form factor of 2.6 is not a necessary condition for separation.

A bursting frequency of $5.3\ kHz$ was found in the incoming boundary layer but that frequency could not be found in the separated region. $5.3\ kHz$ is close to $0.14U_\infty/\delta_{99}$ found in supersonic flows. In the initial separation, a frequency of $1550\ Hz$ dominates, but as the separation evolves, structures of other frequencies are added, some of them can be found also in the incoming boundary layer.

A newly started project at Chalmers aims on making proper orthogonal decomposition POD of the data presented here. Hopefully, the POD can shed some light on what kind of structures that belong to which frequency.

Chapter 7

Future work

Another LES is going to be performed where the inlet boundary data has been improved by using DNS flucutuations that cover the whole inlet. On the outlet, absorbing boundary conditions are going to be implemented and a grid dependent filter width introduced in the subgrid model. Neither of these improvements should have any large effects, but the only way to be sure of such a statement is to run tests.

When all doubts about the quality of the computations have been removed, an LES with higher Reynolds number will be run to investigate the Reynolds number effects.

All of these calculations will give a comprehensive data base which, in cooperation within the STEM program, will be analysed using POD. Results from that analysis will hopfully result in the construction of a subgrid model using POD.

Bibliography

[1] Dolling, D. S., "Fifty Years of Shock-Wave/Boundary-Layer Interaction Research: What Next?" *AIAA Journal*, Vol. 39, No. 8, 2001, pp. 1517 – 1531.

[2] "Shock-Wave Boundary Layer Interactions," AGARDograph No.280, 1986.

[3] Beresh, S., Clemens, N., and Dolling, D., "Relationship Between Upstream Turbulent Boundary-Layer Velocity Fluctuations and Separation Shock Unsteadiness," *AIAA Journal*, Vol. 40, 2002, pp. 2412 – 2422.

[4] Bur, R., Benay, R., Corbel, B., and Dlery, J., "Physical Study of Shock-wave / Boundary-layer interaction control in transonic flow," AIAA Paper, 2000.

[5] Knight, D., Yan, H., Panaras, A. G., and Zheltovodov, A., "Advances in CFD prediction of shock wave turbulent boundary layer interactions," *Progress in Aerospace Science*, Vol. 39, 2003, pp. 122 – 184.

[6] Sandham, N., Yao, Y., and Lawal, A., "Large-eddy simulation of transonic turbulent flow over a bump," *Heat and Fluid Flow*, Vol. 24, 2003, pp. 584 – 595.

[7] Garnier, E., Sagaut, P., and Deville, M., "Large Eddy Simulation of Shock/Boundary-Layer Interaction," *AIAA Journal*, Vol. 40, 2002, pp. 1935 – 1944.

[8] Sigfrids, T., "Hot wire and PIV studies of transonic turbulent wall-bounded flows," Thesis for licentiate of engineering, Department of Mechanics, Royal Institute of Technology, Sweden, 2003.

[9] Bron, O., *Numerical and experimental study of the Shock-Boundary Layer Interaction in Transonic Unsteady Flow*, Ph.D. thesis, Royal Institute of Technology, Sweden, 2003.

[10] Eriksson, L.-E., "Development and validation of highly modular flow solver versions in g2dflow and g3dflow series for compressible viscous reacting flow," Internal report 9970–1162, Volvo Aero Corporation, Sweden, 1995.

[11] Erlebacher, G., Hussaini, M. Y., Speziale, C. G., and Zang, T. A., "Toward the large-eddy simulation of compressible turbulent flows," *Journal of Fluid Mechanics*, Vol. 238, 1992, pp. 155 – 185.

[12] Pope, S. B., *Turbulent flows*, Cambridge university press, Cambridge, United Kingdoms, 2000.

[13] Hoffmann, K. A. and Chiang, S. T., *Computational fluid dynamics for engineers volume II*, Engineering Education System, Wichita, Kansas, USA, 1993.

[14] Laney, C. B., *Computational Gasdynamics*, Cambridge university press, New York, USA, 1998.

[15] Wollblad, C., Davidson, L., and Eriksson, L.-E., "Semi-implicit Preconditioning for Wall-bounded Flow." AIAA conference, 2004, paper number 2004-2135.

[16] Press, W. H., Teukolsky, S. A., Vetterling, W. T., and Flannery, B. P., *Numerical Recipes in Fortran*, Cambridge University Press, 1992.

[17] Rice, J. A., *Mathematical Statistics and Data Analysis*, Duxbury press, Belmont, California, USA, 1995.

[18] Wilcox, D. C., *Turbulence Modeling for CFD*, DCW Industries, Mill Valley, California, USA, 2nd ed., 1998.

[19] Andersson, N., "A Study of Mach 0.75 Jets and Their Radiated Sound Using Large-Eddy Simulation," Thesis for licentiate of engineering, Department of Thermo and Fluid Mechanics, Chalmers, Sweden, 2003.

[20] Welty, J. R., Wicks, C. E., and Wilson, R. E., *Fundamentals of Momentum, Heat, and Mass Transfer*, John Wiley & sons, New York, USA, 1984.

[21] Johansson, G. and Castillo, L., "LDA measurements in turbulent boundary layers with zero pressure gradient," *Proc. Turbulence and Shear Flow Phenomena,* 2^{nd} *International Symposium*, Stockholm, 2001, pp. 15 – 20.

[22] Johansson, T. G. and Karlsson, R. I., "Measurement Issues in High Reynolds Number Flows," AIAA conference, 2002, paper number 2002-1108.

[23] Schlichting, H., *Boundary-Layer Theory, seventh edition*, McGraw-Hill Book Company, New York, USA, 1979.

[24] U.Piomelli and Chasnov, J., "Large-eddy simulations: Theory and applications," *Transition and Turbulence Modelling*, edited by D. Henningson, M. Hallbaeck, H. Alfredsson, and A. Johansson, Kulwer Academic Publisher, 1996, pp. 269–336.

[25] Rotta, J. C., "Statistische Theorie nichthomogener Turbulenz," *Zeitschrift fur Physic*, Vol. 129, 1951, pp. 547 – 572.

[26] Thomas, F. O., Putnam, C. M., and Chu, H. C., "On the mechanism of unsteady shock oscillation in shock wave/turbulent boundary layer interactions," *Experiments in Fluids*, Vol. 18, 1994, pp. 69 – 81.

[27] Andreopoulos, J. and Muck, K., "Some new aspects of the shock-wave/boundary-layer interaction i compression-ramp flows," *AIAA Journal*, Vol. 180, 1987, pp. 405 – 428.

[28] Wu, M. and Martin, M. P., "Direct Numerical Simulation of Shock-wave/Turbulent Boundary Layer Interaction," AIAA conference, 2004, paper number 2004-2145.

[29] Jones, W. and Launder, B., "The Prediction of Laminarization with a Two-equation Model of Turbulence," *International Journal of Heat and Mass Transfer*, Vol. 15, 1971, pp. 301 – 314.

[30] Castillo, L., Wang, X., and George, W. K., "Separation Criterion for Turbulent Boundary Layers Via Similarity Analysis," *Journal of Fuids Engineering*, Vol. 126, 2004, pp. 297 – 304.

[31] Ichimiya, M., Nakamura, I., and Yamashita, S., "Properties of a relaminarizing turbulent boundary layer under a favorable pressure gradient," *Experimental Thermal and Fluid Science*, Vol. 17, 1997, pp. 37 – 48.

Included Paper

C. Wollblad, L. E. Eriksson and L. Davidson,
”Semi-implicit Preconditioning for Wall-bounded Flow.”,
34th AIAA Fluid Dynamics Conference and Exhibit, AIAA 2004-2135
Portland, Oregon, 2004.